

2017

Investigating the Charge-Transfer Dynamics of Single-Molecule Sensitizers

Jenna Tan

College of William and Mary, jatan@email.wm.edu

Follow this and additional works at: <https://scholarworks.wm.edu/etd>

 Part of the [Chemistry Commons](#)

Recommended Citation

Tan, Jenna, "Investigating the Charge-Transfer Dynamics of Single-Molecule Sensitizers" (2017). *Dissertations, Theses, and Masters Projects*. Paper 1516639563. <http://dx.doi.org/doi:10.21220/S2QQ2K>

This Thesis is brought to you for free and open access by the Theses, Dissertations, & Master Projects at W&M ScholarWorks. It has been accepted for inclusion in Dissertations, Theses, and Masters Projects by an authorized administrator of W&M ScholarWorks. For more information, please contact scholarworks@wm.edu.

Investigating the Charge-Transfer Dynamics of Single-Molecule Sensitizers

Jenna Adrienne Uy Tan

Virginia Beach, Virginia

Bachelor of Science, College of William and Mary, 2016

A Thesis presented to the Graduate Faculty
of The College of William & Mary in Candidacy for the Degree of
Master of Science

Department of Chemistry

College of William & Mary
August, 2017

APPROVAL PAGE

This Thesis is submitted in partial fulfillment of
the requirements for the degree of

Master of Science



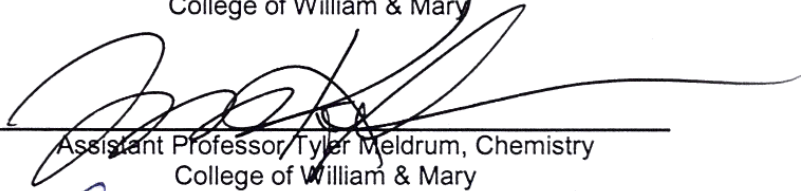
Jenna A. Tan

Approved by the Committee, April 2017

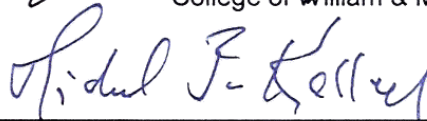


Committee Chair

Associate Professor Kristin Wustholz, Chemistry
College of William & Mary



Assistant Professor Tyler Meldrum, Chemistry
College of William & Mary



Professor Michael Kelley, Applied Science
College of William & Mary

ABSTRACT

Dye-sensitized solar cells (DSSCs) can reduce the cost of photovoltaic electricity generation to meet global energy needs. Optimizing DSSC efficiency requires a detailed understanding of the underlying charge transfer processes at the dye-semiconductor interface. By modifying the sensitizer structure, we gain insight into these charge transfer mechanisms. In this thesis, two hydroxyanthraquinone dyes are compared to investigate the impact of structure on charge-transfer and photobleaching dynamics. A combination of ensemble-averaged and single-molecule spectroscopy approaches are used to interpret the underlying ET kinetics.

TABLE OF CONTENTS

Acknowledgements	ii
Dedications	iii
List of Tables	iv
List of Figures	v
List of Abbreviations	vi
Chapter 1. Introduction:	
Sustainable Energy for the Future	1
Impact of Sensitizer on Dye-Sensitized Solar Cell Performance	3
Single-molecule spectroscopy	7
Statistical Interpretation of Blinking Dynamics	10
Thesis Outline	13
References	15
Chapter 2. Contributions from Excited-State Proton and Electron Transfer to the Blinking and Photobleaching Dynamics of Alizarin and Purpurin:	
Introduction	18
Experimental	21
Results and Discussion	23
Conclusion	40
Acknowledgements	42
References	43
Appendix I. Fluorescence Blinking as an Output for Programmable Biosensing	46
Appendix II. Time-Related Single Photon Counting Studies for Sensitizers.	63

ACKNOWLEDGEMENTS

I am thankful to my advisor and mentor, Dr. Wustholz, for her steadfast encouragement and patience throughout my research endeavors over the past 5 years. It is through her guidance that I have developed my scientific perspective and skills as well as valuable outlooks on life. Thank you for taking a chance on me as a freshman lab volunteer. I am also appreciative of Dr. Meldrum and Dr. Kelley for their time and review of the manuscript. Thank you to Dr. Bebout and Dr. Pike for their guidance through the M.S. program.

I would like to acknowledge the support I had from fellow members in the Wustholz Lab. I am especially grateful for the mentorship of Natalie Wong and Alana Ogata, and to my teammates Simran Rohatgi, Seth Greenspan, and James Cassidy. Your questions and conversations challenged me to continually deepen my knowledge about our projects and approach ideas from different angles.

Thank you to James, Shelle Butler, and Jonathan Perkins for making my M.S. research period filled with laughter and camaraderie.

Special thanks to Mom, Dad, Joanna, and John for supporting me to the end.

To Mom, Dad, and Joanna.

LIST OF TABLES

1.	Best-fit parameters for on- and off-interval distributions of alizarin and purpurin	31
2.	Log-likelihood ratio test results	33

LIST OF FIGURES

1.	Schematic of Dye-Sensitized Solar Cell	3
2.	Normalized Rate Areas of Charge-Transfer Kinetics	5
3.	Structures of Alizarin and Purpurin	6
4.	Single Molecule Scan and Blinking Dynamics	9
5.	Blinking Traces of Alizarin and Purpurin	24
6.	Ensemble-Averaged Fluorescence Spectra	26
7.	On- and off-interval Probability Distributions	28
8.	Intensity Histogram of Photobleaching Event	36
9.	Off-Event Probability Distributions	37
10.	Proposed Blinking and Photobleaching Mechanisms	39
11.	Single Quantum Dot Scans and Blinking Dynamics	47
12.	Biosensing Schematic	48
13.	Recognition of Target Nucleic Acids by biosensor	50
14.	Streaking of Quantum Dot Scans	53
15.	Blinking Dynamics of Quantum Dot biosensors	55
16.	Blinking Dynamics of Quantum Dot Biosensors with Different Preparations	56
17.	Normalized Fluorescence Decay of Rhodamine 560	77

LIST OF ABBREVIATIONS

BET: Back electron transfer
CPD: Change-point detection
CT: Charge transfer
CW: Continuous wavelength
DSSC: Dye-sensitized solar cell
ESIPT: Excited-state intramolecular proton transfer
ET: Electron transfer
IRF: Instrument-response function
ISC: Intersystem crossing
KS: Kolmogorov-Smirnov
LLR: Log-likelihood ratio
MLE: Maximum-likelihood estimation
PT: Proton transfer
QD: Quantum dot
SMS: Single-molecule spectroscopy
SNR: Signal-to-noise ratio
TCSPC: Time-correlated single-photon counting

CHAPTER 1: INTRODUCTION

Sustainable Energy for the Future

Advancements in human civilization are driven by our ability to harness energy. We transformed global transportation and trade by using natural resources, such as fire and coal, to power engines and provide for electricity. Currently, fossil fuel sources supply approximately 80% of the world's energy needs.¹ Although fossil fuels have given the impetus for technological and economic growth, they are also responsible for over 75% of global CO₂ emissions.¹ The emission of CO₂ has been linked to a drastic increase in global temperatures and adverse climate effects such as rising sea levels and droughts.^{2,3} In order to mitigate human-induced climate change, 197 nations pledged to curb the global temperature rise to no more than 2°C by the end of this century by reducing CO₂ emissions from the energy sector.² The benchmark of two degrees represents the point beyond which humans can no longer control climate change effects. Meeting this goal will be challenging since energy demands are concurrently expected to increase ~33% due to population growth within the century.^{3,4} Although fossil fuels will continue to supply humans in the short term, the path toward a sustainable future will be dictated by our investment in alternative energy sources.

In short, an energy revolution is needed, where new energy sources are developed that are sustainable and emission-free.³ Renewable energy sources are derived directly or indirectly from the sun or from natural movements in the environment (i.e., geothermal or tidal).⁵ Altogether, renewable energy sources

can provide over 3000 times the current global energy needs if harnessed effectively.⁵⁻⁷ Solar energy is the leading option because of its enormous abundance. Of the 170,000 TW worth of solar energy that strikes the earth's surface, approximately 600 TW can be harvested, which would exceed global energy demands 200 times over.⁸ The sun's vast potential of solar energy has fueled motivation for solar technology development. Photovoltaic devices harness solar energy for electricity conversion based upon the principle of charge separation at conductive materials interfaces.^{8,9} Although conventional silicon-based photovoltaics have reduced solar-generated electricity prices to 0.07 US\$•kWh⁻¹, silicon solar cells remain cost-prohibitive to the public due to the price of crystalline silicon and complex production techniques.⁹ Furthermore, the toxicity and low abundance of materials are problematic for conventional solar cells. In order to be more competitive with cheap fossil fuels, the cost of solar-generated electricity needs to decrease to 0.02 US\$•kWh⁻¹,⁹ which will require innovative designs that improve efficiency of solar cells and reduce their production costs.

In recent years, dye-sensitized solar cells (DSSCs) have emerged as an economically and technically-viable alternative to silicon-based solar cells. DSSCs are made of earth-abundant materials, which result in lower production costs relative to silicon solar cells. Furthermore, DSSCs are more mechanically robust yet flexible, which provides opportunities for commercial integration.^{8, 10-13} DSSCs also demonstrate improved performance in real world conditions under diffuse light (i.e., when the sky is not completely clear) and higher temperatures.

With all of these valuable properties, there has been considerable research and development to optimize the various DSSC components. However, implementing DSSCs on a global scale will require improved materials design based on fundamental insights.

Impact of Sensitizer on Dye-Sensitized Solar Cell Performance

DSSCs have enormous potential to reduce the cost of photovoltaic electricity generation for the public. Modern DSSCs are composed of dye sensitizers that are adsorbed onto a semiconductor film in the presence of an electrolyte, all of which are sandwiched between a transparent conductive oxide and counter electrode (Figure 1).^{8, 10-13} Photoexcitation of the dye produces an excited electron, which is injected into the conduction band of the semiconductor (e.g., TiO_2 , ZnO) and converted into electricity at the electrode. The oxidized dye is regenerated to its ground state through electron donation by an electrolyte in order to sustain the photovoltaic process.

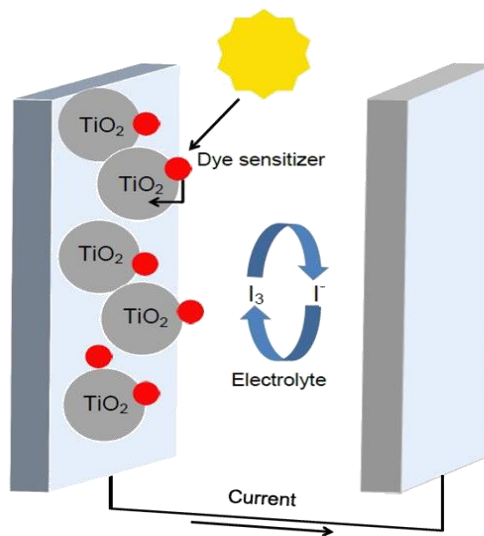


Figure 1. Schematic of a dye-sensitized solar cell (DSSC). Dye sensitizer (red) is adsorbed onto a semiconductor nanoparticle, typically titanium dioxide (TiO_2 , silver). Electrolyte is embedded to regenerate the dye sensitizer. The electron is converted into electricity at the electrode.

A crucial difference between the DSSC and silicon solar cell lays in the charge separation and transfer processes. Unlike a silicon solar cell, the DSSC is composed of two different materials to carry out light absorption and electron transport. The dye sensitizer is responsible for light absorption, while the semiconductor and electrolyte transport electrons. Consequently, the dye sensitizer controls the light-harvesting capacity of the DSSC.¹⁴ Successful dye sensitizers have high molar extinction coefficients in the visible and near-IR ranges, strong anchoring groups (i.e., -COOH, -H₂PO₃, -OH, etc.) to bind to the semiconductor, and appropriate HOMO and LUMO levels for injection into the semiconductor.^{8,12,14-16} The most popular dye sensitizers are based on ruthenium complexes, where they have increased DSSC efficiency to ~11% due to efficient metal-to-ligand charge transfer (CT) transition between the p* orbitals of ruthenium and TiO₂.^{8,10,11} However, ruthenium is a relatively rare and expensive material, which would make DSSC production impractical for large-scale commercialization.⁸⁻¹⁵ As a result, organic dye sensitizers are being pursued as alternatives to ruthenium-based sensitizers. Since these non-metal sensitizers are relatively inexpensive, have facile tunable absorption properties, large molar extinction coefficients, and are more environmentally friendly, they present a promising opportunity toward designing a cost-effective DSSC.^{16,17}

Organic dye sensitizers offer infinite possibilities for improving properties such as efficient light harvesting or charge separation by modifying the structure. Coumarin,^{18,19} indoline,²⁰ conjugated oligo-ene,²¹ and xanthene^{22,23} dyes represent organic dye sensitizers that have made substantial progress in

improved device efficiencies that match those of ruthenium-based sensitizers. Despite the potential of organic dye sensitizers to effectively harvest light in DSSCs, there are significant challenges that impact the performance of organic dyes in DSSCs: complex photophysics and photostability. Figure 2 provides an illustration of the areas of normalized rates for the various CT kinetics that involve the sensitizer.²⁴ These kinetics span multiple timescales and are dispersive, which introduces kinetic competition between various CT processes. Previous studies have shown that organic dye sensitizer photophysics are difficult, complex, and multiphasic due in part to the sensitizer structure and heterogeneous local environment of the dye molecule.²⁵⁻²⁷ Heterogeneous CT kinetics contribute to inefficiency in DSSCs; yet, the underlying photophysical processes remain poorly understood.

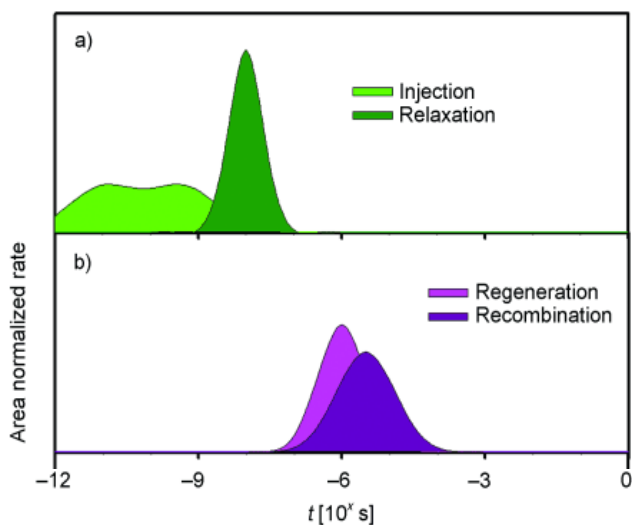


Figure 2. The normalized rate areas and timescales of charge transfer (CT) processes that involve the dye sensitizer.²⁴

Organic dyes also demonstrate photostability issues when incorporated into complex environments like fabric, art, or DSSCs. Photostability describes the

likelihood of an excited molecule to undergo degradation pathways rather than returning to the ground state through non-degradative modes.²⁸ When exposed to oxygen or ultraviolet radiation, organic dyes often degrade over time.²⁹ On textiles, these organic dyes would often be mixed with a photostabilising agent or metal mordant in order to remain colorfast.^{28,29} With DSSC preparation, the organic dye sensitizers are prepared in an inert environment in order to preserve the photostability of the device.²⁹ However, preparing organic dyes in photostabilising agents or an inert environment do not prevent the eventual photodegradation of the organic dye. Although qualitative observations about the photostability and degradation of the organic dyes have been tracked, a more mechanistic understanding of photostability is required to incorporate stable sensitizers for sustainable DSSCs.

Alizarin (1,2-dihydroxyanthraquinone) and purpurin (1,2,4-trihydroxyanthraquinone) are two well-known organic dyes (Figure 3) that have been explored for use as potential dye sensitizers. Their interesting photophysical properties and ability to form coordination complexes with TiO_2 provide a perspective to better understand molecular principles in DSSC performance.³⁰

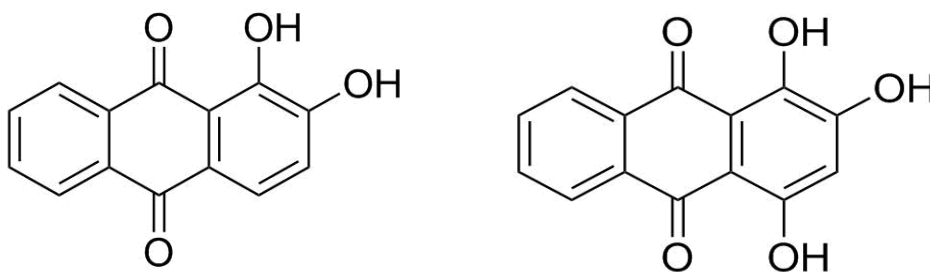


Figure 3. Structures of alizarin (left, 1,2-dihydroxyanthraquinone) and purpurin (right, 1,2,4-trihydroxyanthraquinone). The hydroxyl functional groups anchor to the TiO_2 semiconductor.

For example, a study on alizarin coupled to TiO₂ revealed insights into CT processes such as electron injection from the excited sensitizer state into the conduction band of TiO₂.³¹ Kaniyankandy et al. discovered that electron injection occurred on multiple timescales, which illustrated the complexity of sensitizer photophysics.³¹ Furthermore, Kaniyankandy et al. gained insight into the orbital overlap between alizarin and TiO₂.³¹ Alizarin and purpurin have strikingly similar structures but exhibit distinct photophysical and photochemical properties, where alizarin is observed to be more photostable than purpurin. These two dyes present the opportunity to understand the underlying complex photophysics and differences in photostability in organic dyes. While ensemble-averaged techniques provide averaged information about CT and a general characterization of the operating CT processes, these methods obscure the complexity of nanoscale behavior. Single-molecule spectroscopy (SMS) provides the ability to probe the impact of local environment and structure on CT dynamics and photostability at the single-molecule level. This thesis will employ SMS to yield the photophysical processes underlying the CT dynamics of sensitizers with similar structures yet different photostabilities.

Single-Molecule Spectroscopy

Single-molecule spectroscopy (SMS) is a critical tool in modern scientific studies that probes the ensemble average to reveal the complete distribution of nanoscale dynamics. The complexity and heterogeneity of the photophysics of organic dyes makes it difficult for bulk characterization to fully analyze CT

kinetics. Previous studies demonstrate that interfacial CT dynamics are better understood with SMS by determining how the structure of the sensitizer influences electronic coupling with and binding orientation onto the semiconductor.³²⁻³⁸ Since single molecules can “act as local reporters on their nanoenvironment,”³⁶ SMS studies reveal insight into the hidden details under ensemble-averaged measurements to connect the local environment with CT kinetics. SMS reveals the full distribution of CT dynamics, rather than a single number given by ensemble-averaged measurements.

Achieving single-molecule resolution relies on two essential principles: to guarantee that only one molecule will be photoexcited within a certain volume and that the signal-to-noise ratio (SNR) is greater than unity over the averaging time.³⁶ Additional measures taken to ensure single-molecule resolution include the observation of a diffraction-limited spot and photobleaching, which is when a molecule is irreversibly transformed into a non-fluorescent complex.³⁹⁻⁴¹ Establishing a single molecule within a certain volume will require concentration studies to figure out the proper dilution, while finding the appropriate SNR can take a few approaches, which for the most part is dependent upon the fluorophore of choice. To obtain a large signal, a small focal volume, large absorption cross section, and a high fluorescence quantum yield are ideal for SM studies.³⁶ False-colored fluorescence images of single molecules can be obtained under laser excitation with a raster scanning pattern (Figure 4). Once the single molecules have been identified in the image, they are observed under continuous excitation. Although steady fluorescence from a fluorophore is

expected, single molecules that are not photostable can exhibit fluctuations in emission and even photobleaching. These single-molecule properties can provide valuable insight into the underlying photophysics of organic dye sensitizers.

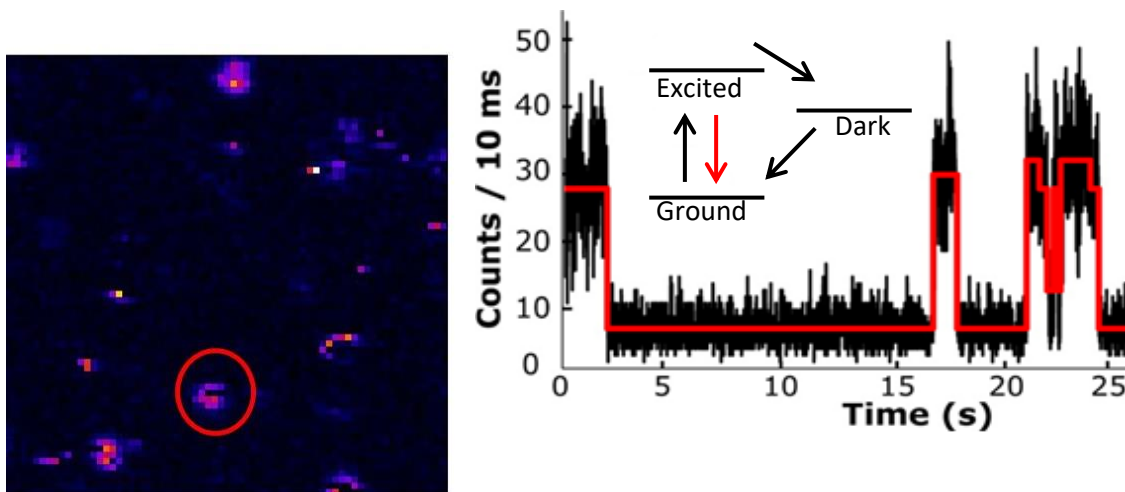


Figure 4. (Left) $7 \times 7 \mu\text{m}^2$ false-colored fluorescent image of organic dye molecules on TiO_2 are detected.⁴⁰ Once a molecule is located (red circle), continuous excitation induces blinking dynamics (right). Intensity counts are photons detected from fluorescence. Threshold analysis (red line) determines the on and off states of each blinking trace.

Single-molecule photophysics are probed by measuring emissive (i.e., on state) and non-emissive (i.e., off state) events from single molecules.⁴²⁻⁴⁹ This single-molecule phenomenon is known as blinking, where the fluctuations in emissive intensities are due to the population and depopulation of optically bright- and dark-vibronic states (Figure 4). Appendix I outlines a study on the application of blinking with quantum-dot (QD) biosensors, where binary blinking from single QDs is observed until the biosensor reaches its target RNA strand.⁵⁰ Blinking can be modeled by a three-level system, where the fluorescence is modeled by rate equations. Emissive events occur when a molecule undergoes fluorescence, which is illustrated in Figure 4 (i.e., emission of photons after

relaxation to the ground state), and non-emissive events represent transfer into a dark state, where the molecule can then repopulate the ground state and cycle through the process all over again.

Unique blinking dynamics from single molecules provide us the opportunity to probe underlying photophysical mechanisms and even observe the death of a molecule, i.e. photobleaching. Previous studies have been able to connect blinking to the underlying CT kinetics between a dye sensitizer and semiconductor.^{39-41,51,52} Being able to interpret the dispersive CT kinetics lends greater insight into the interaction between the dye sensitizer and its local environment, as well as the impact of the sensitizer structure on photophysics. Moreover, blinking can reveal the impact of structure and photophysics on photostability through photobleaching events. Single-molecule data offers the opportunity to unravel complex photophysics of organic dye sensitizers and observe differences in photostability. However, blinking dynamics require rigorous statistical analysis in order to thoroughly understand the underlying physical mechanisms.

Statistical Interpretation of Blinking Dynamics

Single-molecule blinking dynamics are quantified to connect variations in fluorescence with CT kinetics. Applying a uniform threshold to determine on and off states is prone to error because molecules have been observed to emit multiple emissive intensities within a blinking trace.^{40,41,51-53} Instead, the durations of the on and off states (i.e., on times and off times, respectively) obtained from blinking dynamics are determined by a rigorous change point detection (CPD)

algorithm.⁵³ By using the CPD algorithm, we can statistically identify whether an intensity is considered an emissive (on) or non-emissive (off) state.^{40,41,53} The algorithm can also determine the time of photobleaching for a molecule.⁵⁴ Once the hundreds of blinking dynamics of have been analyzed for on and off state durations, they are compiled into histograms and fit by probability functions. The probability function that best fits the on- and off-time distributions can reveal information about the population and de-population of the dark state, respectively.^{40,41,54} When blinking occurs through a triplet state, the population and de-population processes of the triplet state follow first-order kinetics and are described by exponential functions. First-order rate constants for intersystem crossing (ISC) into the triplet state and decay to the ground state can be extracted from the exponential fits.⁵⁵⁻⁵⁷

Several single-molecule studies report that the CT kinetics do not always follow first-order kinetics. Instead, dispersive CT kinetics are observed, which indicates that the rate constants for population and de-population of the non-emissive state evolve over time.^{39-41,51-59} Several studies observe that on and off-time distributions are best fit by the power-law model, which is characterized as a straight line on log-log axes.⁶⁰ Although power laws are thought to universally describe blinking, recent studies have increasingly shown that blinking may not be power-law distributed.^{40,41,51,52,54} For example, Mitsui et al. investigated perylenediimide single molecules to evaluate intersystem crossing (ISC) and CT processes between the dye and polymer matrix.⁵² They discovered that the on-time and off-time distributions were described by alternatives to the power-law

distribution: Weibull and lognormal, respectively. These heavy-tailed functions reveal insight into the ISC and CT processes, where Mitsui et al. could determine the likelihood of ISC with increased time as well as consider the distribution of driving forces for CT. Handling single-molecule data requires careful and rigorous evaluation in order to determine the true underlying distribution that will describe the single-molecule photophysics.

Clauset et al. describe a set of statistical techniques to confidently conclude if a distribution is described by the power-law or an alternative distribution.⁶⁰ With this proposed method, we depart from the least-squares fitting method on the probability density function of a data set, which demonstrates systematic errors, underestimates the power-law exponent, and does not provide a test to determine the likelihood of a power law describing the data.^{40,60} In order to avoid the shortcomings of the least-squares fitting method, Clauset et al. propose the use of the maximum-likelihood estimation (MLE) method on the cumulative distribution function to determine fit parameters. Once the fit parameters have been determined, the goodness-of-fit and p-value is calculated, according to the Kolmogorov-Smirnov test, in order to determine the likelihood of the fit parameters to the distribution.⁶⁰ Finally, a likelihood ratio test or alternative statistical test is used to determine if another distribution can be considered relative to your null distribution.⁶⁰ This combined MLE/KS approach will ensure that dispersive kinetics will be rigorously described by the appropriate function.

Recently, we studied a series of rhodamine dyes on TiO₂ to determine the effects of dye structure, driving force, and TiO₂ adsorption affinity on the

photophysics of rhodamine dyes.⁴¹ With the MLE/KS approach, our on- and off-time distributions were determined to be described by the log-normal distribution, which was consistent with a Gaussian-distribution of activation energy barriers. By demonstrating that power-law distributions are not a universal blinking feature, we can use the fit parameters of the alternative distributions to better interpret photophysics. Additional studies demonstrated the importance of using robust statistical tests to interpret blinking measurements, since differences in fitting methods can produce varied interpretations of the same data.^{40,51,52}

Thesis Outline

This thesis focuses on the SMS studies on the photophysics and photobleaching dynamics of dye sensitizers on glass substrate. Alizarin (1,2-dihydroxyanthraquinone) and purpurin (1,2,4-trihydroxyanthraquinone) are two organic dyes that have historically been used in paintings but have recently gained attention as potential sensitizers for DSSCs. Despite their similar structures, alizarin and purpurin demonstrate different photostabilities, where alizarin is more photostable than purpurin. Our SMS results revealed that excited-state intramolecular proton transfer (ESIPT) and ET are both operative in alizarin, while purpurin can only undergo ET. Furthermore, analysis of the photobleaching events in alizarin and purpurin demonstrated that the probability of photobleaching increases with the time spent in the radical cation state. By combining the blinking and photobleaching analyses, we proposed that alizarin is less likely to photobleach since it can undergo ESIPT instead of ET to the radical

cation state. In contrast, purpurin can only undergo ET, so purpurin is more likely to reside in the radical cation state and photobleach. These SMS studies lay the foundation for improved SM studies as we incorporate the time-correlated single photon counting (TCSPC) technique with our SMS approach. In Appendix II, we outline TCSPC guidelines for conducting studies and fitting lifetime decays.

References

1. Hosenuzzaman, M., Rahim, N.A., Selvaraj, J., Hasanuzzaman, M., Malek, A.B.M.A. and Nahar, A. Global prospects, progress, policies, and environmental impact of solar photovoltaic power generation. *Renewable and Sustainable Energy Reviews*, **2015**, 41, 284-297.
2. Gielen, D., Boshell, F. and Saygin, D. Climate and energy challenges for materials science. *Nature materials*, **2016**, 15(2), 117-120.
3. Chu, S. and Majumdar, A. Opportunities and challenges for a sustainable energy future. *Nature*, **2012**, 488, 294 – 303.
4. Khan, M.A., Khan, M.Z., Zaman, K. and Naz, L. Global estimates of energy consumption and greenhouse gas emissions. *Renewable and Sustainable Energy Reviews*, **2014**, 29, 336-344.
5. Ellabban, O., Abu-Rub, H. and Blaabjerg, F. Renewable energy resources: Current status, future prospects and their enabling technology. *Renewable and Sustainable Energy Reviews*, **2014**, 39, 748-764.
6. Sahu, B.K. A study on global solar PV energy developments and policies with special focus on the top ten solar PV power producing countries. *Renewable and Sustainable Energy Reviews*, **2015**, 43, 621-634.
7. Devabhaktuni, V., Alam, M., Depuru, S.S.S.R., Green, R.C., Nims, D. and Near, C. Solar energy: Trends and enabling technologies. *Renewable and Sustainable Energy Reviews*, **2013**, 19, 555-564.
8. Hagfeldt, A., Boschloo, G., Sun, L., Kloo, L. and Pettersson, H. Dye-sensitized solar cells. *Chemical reviews*, **2010**, 110(11), 6595-6663.
9. Chu, S., Cui, Y. and Liu, N. The path towards sustainable energy. *Nature Materials*, **2017**, 16(1), 16-22.
10. Gratzel, M. Conversion of Sunlight to Electrical Power by nanocrystalline dye-sensitized solar cells. *Journal of Photochemistry and Photobiology A: Chemistry*. **2004**, 164, 3-14.
11. Nazeeruddin, M.K., Baranoff, E. and Grätzel, M. Dye-sensitized solar cells: a brief overview. *Solar Energy*, **2011**, 85(6), 1172-1178.
12. Listorti, A., O'Regan, B. and Durrant, J.R. Electron transfer dynamics in dye-sensitized solar cells. *Chemistry of Materials*, **2011**, 23(15), 3381-3399.
13. Lee, J.K. and Yang, M. Progress in light harvesting and charge injection of dye-sensitized solar cells. *Materials Science and Engineering: B*, **2011**, 176(15), 1142-1160.
14. Clifford, J.N., Martínez-Ferrero, E., Viterisi, A. and Palomares, E. Sensitizer molecular structure-device efficiency relationship in dye sensitized solar cells. *Chemical Society Reviews*, **2011**, 40(3), 1635-1646.
15. Mathew, S., Yella, A., Gao, P., Humphry-Baker, R., Curchod, B.F., Ashari-Astani, N., Tavernelli, I., Rothlisberger, U., Nazeeruddin, M.K. and Grätzel, M. Dye-sensitized solar cells with 13% efficiency achieved through the molecular engineering of porphyrin sensitizers. *Nature chemistry*, 6(3), 242-247.
16. Mishra, A., Fischer, M.K. and Bäuerle, P., 2009. Metal-free organic dyes for dye-sensitized solar cells: From structure: Property relationships to design rules. *Angewandte Chemie International Edition*, **2014**, 48(14), 2474-2499.
17. Lee, J.K. and Yang, M. Progress in light harvesting and charge injection of dye-sensitized solar cells. *Materials Science and Engineering: B*, **2011**, 176(15), 1142-1160.
18. Koops, S.E., Barnes, P.R., O'regan, B.C. and Durrant, J.R. Kinetic competition in a coumarin dye-sensitized solar cell: injection and recombination limitations upon device performance. *JPCA*, **2011**, 114(17), 8054-8061.
19. Seo, K.D., Song, H.M., Lee, M.J., Pastore, M., Anselmi, C., De Angelis, F., Nazeeruddin, M.K., Grätzel, M. and Kim, H.K. Coumarin dyes containing low-band-gap chromophores for dye-sensitized solar cells. *Dyes and Pigments*, **2011**, 90(3), 304-310.
20. Ding, W.L., Wang, D.M., Geng, Z.Y., Zhao, X.L. and Yan, Y.F. Molecular engineering of indoline-based D-A- π -A organic sensitizers toward high efficiency performance from first-principles calculations. *JPCA*, **2013**, 117(34), 17382-17398.

21. Hwang, S., Lee, J.H., Park, C., Lee, H., Kim, C., Park, C., Lee, M.H., Lee, W., Park, J., Kim, K. and Park, N.G. A highly efficient organic sensitizer for dye-sensitized solar cells. *Chemical Communications*, **2007**, (46), 4887-4889.
22. Zhang, F., Shi, F., Ma, W., Gao, F., Jiao, Y., Li, H., Wang, J., Shan, X., Lu, X. and Meng, S. Controlling adsorption structure of Eosin Y dye on nanocrystalline TiO₂ films for improved photovoltaic performances. *JPCC*, 2013, 117(28), 14659-14666
23. Ferreira, E.S., Hulme, A.N., McNab, H. and Quye, A. The natural constituents of historical textile dyes. *Chemical Society Reviews*, **2004**, 33(6), 329-336.
24. Martinson, A.B., Hamann, T.W., Pellin, M.J. and Hupp, J.T. New Architectures for Dye-Sensitized Solar Cells. *Chemistry-A European Journal*, **2008**, 14(15), 4458-4467.
25. Lee, J.W., Hwang, K.J., Shim, W.G., Park, K.H., Gu, H.B. and Kwun, K.H. Energetic surface heterogeneity of nanocrystalline TiO₂ films for dye-sensitized solar cells. *Korean Journal of Chemical Engineering*, **2007**, 24(5), 847-850.
26. Ardo, S. and Meyer, G.J. Photodriven heterogeneous charge transfer with transition-metal compounds anchored to TiO₂ semiconductor surfaces. *Chemical Society Reviews*, **2009**, 38(1), 115-164.
27. Kaniyankandy, S., Verma, S., Mondal, J.A., Palit, D.K. and Ghosh, H.N. Evidence of multiple electron injection and slow back electron transfer in alizarin-sensitized ultrasmall TiO₂ particles. *JPCC*, **2009**, 113(9), 3593-3599.
28. Manian, A.P., Paul, R. and Bechtold, T. Metal mordanting in dyeing with natural colourants. *Coloration Technology*, **2016**, 132(2), 107-113.
29. Hug, H., Bader, M., Mair, P. and Glatzel, T. Biophotovoltaics: natural pigments in dye-sensitized solar cells. *Applied Energy*, **2014**, 115, 216-225.
30. Li, C., Yang, X., Chen, R., Pan, J., Tian, H., Zhu, H., Wang, X., Hagfeldt, A. and Sun, L. Anthraquinone dyes as photosensitizers for dye-sensitized solar cells. *Solar Energy Materials and Solar Cells*, **2007**, 91(19), 1863-1871.
31. Kaniyankandy, S., Verma, S., Mondal, J.A., Palit, D.K. and Ghosh, H.N. Evidence of multiple electron injection and slow back electron transfer in alizarin-sensitized ultrasmall TiO₂ particles. *JPCC*, **2009**, 113(9), 3593-3599.
32. Imahori, H., Umeyama, T. and Ito, S. Large π -aromatic molecules as potential sensitizers for highly efficient dye-sensitized solar cells. *Accounts of Chemical Research*, **2009**, 42(11), 1809-1818.
33. Brown, D.G., Schauer, P.A., Borau-Garcia, J., Fancy, B.R. and Berlinguette, C.P. Stabilization of ruthenium sensitizers to TiO₂ surfaces through cooperative anchoring groups. *JACS*, **2015**, 135(5), 1692-1695.
34. Moerner, W.E. Nobel Lecture: Single-molecule spectroscopy, imaging, and photocontrol: Foundations for super-resolution microscopy. *Reviews of Modern Physics*, **2015**, 87, 1183-1212.
35. Moerner, W.E. A dozen years of single-molecule spectroscopy in physics, chemistry, and biophysics. *JPCB*, **2002**, 106, 910-927.
36. De Angelis, F., Fantacci, S., Selloni, A., Nazeeruddin, M.K. and Grätzel, M. First-principles modeling of the adsorption geometry and electronic structure of Ru (II) dyes on extended TiO₂ substrates for dye-sensitized solar cell applications. *JPCC*, 2012, 114(13), 6054-6061.
37. Lee, K.E., Gomez, M.A., Elouatik, S. and Demopoulos, G.P.. Further understanding of the adsorption mechanism of N719 sensitizer on anatase TiO₂ films for DSSC applications using vibrational spectroscopy and confocal Raman imaging. *Langmuir*, **2012**, 26(12), 9575-9583.
38. Ambrosio, F.; Martsinovich, N.; Troisi, A. What Is the Best Anchoring Group for a Dye in a Dye-Sensitized Solar Cell? *JPCL*, **2012**, 3, 1531-1535.
39. Hoogenboom, J.P., Hernando, J., van Dijk, E.M., van Hulst, N.F. and García-Parajó, M.F. Power-Law Blinking in the Fluorescence of Single Organic Molecules. *ChemPhysChem*, **2007**, 8(6), 823-833.
40. Wong, N.Z., Ogata, A.F. and Wustholz, K.L. Dispersive Electron-Transfer Kinetics from Single Molecules on TiO₂ Nanoparticle Films. *JPCC*, **2013**, 117(41), 21075-21085.
41. Tan, J.A., Rose, J.T., Cassidy, J.P., Rohatgi, S.K. and Wustholz, K.L. Dispersive Electron-Transfer Kinetics of Rhodamines on TiO₂: Impact of Structure and Driving Force on Single-Molecule Photophysics. *JPCC*, **2016**, 120(37), 20710-20720.

42. Orrit, M., Ha, T. and Sandoghdar, V. Single-molecule optical spectroscopy. *Chemical Society Reviews*, **2014**, 43(4), 973-976.
43. Barkai, E., Jung, Y. and Silbey, R. Theory of single-molecule spectroscopy: beyond the ensemble average. *Annu. Rev. Phys. Chem.*, **2004**, 55, 457-507.
44. Hess, C.M., Rudolph, A.R. and Reid, P.J. New tools for elucidating the environmental origins of single molecule photoluminescence intermittency. *Chemical Physics Letters*, **2015**, 628, 101-107.
45. Yeow, E.K., Melnikov, S.M., Bell, T.D., De Schryver, F.C. and Hofkens, J. Characterizing the fluorescence intermittency and photobleaching kinetics of dye molecules immobilized on a glass surface. *JPCA*, **2006**, 110(5), 1726-1734.
46. Lin, H., Camacho, R., Tian, Y., Kaiser, T.E., Wurthner, F. and Scheblykin, I.G. Collective fluorescence blinking in linear J-aggregates assisted by long-distance exciton migration. *Nano letters*, **2009**, 10(2), 620-626.
47. Goldberg, J.M., Batjargal, S., Chen, B.S. and Petersson, E.J. Thioamide quenching of fluorescent probes through photoinduced electron transfer: mechanistic studies and applications. *JACS*, **2013**, 135(49), 18651-18658.
48. Warnan, J., Gardner, J., Le Pleux, L., Petersson, J., Pellegrin, Y., Blart, E., Hammarström, L. and Odobel, F. Multichromophoric sensitizers based on squaraine for NiO based dye-sensitized solar cells. *JPCA*, **2013**, 118(1), 103-113.
49. Leng, H., Loy, J., Amin, V., Weiss, E.A. and Pelton, M. Electron Transfer from Single Semiconductor Nanocrystals to Individual Acceptor Molecules. *ACS Energy Letters*, **2016**, 1(1), 9-15.
50. Roark, B., Tan, J.A., Ivanina, A., Chandler, M., Castaneda, J., Kim, H.S., Jawahar, S., Viard, M., Talic, S., Wustholz, K.L. and Yingling, Y.G. Fluorescence blinking as an output signal for biosensing. *ACS Sensors*, 1(11), **2016**, 1295-1300.
51. Riley, E.A., Hess, C.M., Pioquinto, J.R.L., Kaminsky, W., Kahr, B. and Reid, P.J. Proton transfer and photoluminescence intermittency of single emitters in dyed crystals. *JPCB*, **2012**, 117(16), 4313-4324.
52. Mitsui, M., Unno, A. and Azechi, S.. Understanding Photoinduced Charge Transfer Dynamics of Single Peryleneimide Dyes in a Polymer Matrix by Bin-Time Dependence of their Fluorescence Blinking Statistics. *JPCA*, **2016**, 120(28), 15070-15081.
53. Watkins, L.P. and Yang, H. Detection of intensity change points in time-resolved single-molecule measurements. *JPCB*, **2005**, 109(1), 617-628.
54. Tan, J.A., Garakyaraghi, S., Tagami, K.A., Frano, K.A., Crockett, H.M., Ogata, A.F., Patterson, J.D. and Wustholz, K.L. Contributions from Excited-State Proton and Electron Transfer to the Blinking and Photobleaching Dynamics of Alizarin and Purpurin. *JPCA*, **2017**, 121(1), 97-106.
55. Kulzer, F., Xia, T. and Orrit, M. Single molecules as optical nanoprobe for soft and complex matter. *Angewandte Chemie International Edition*, **2010**, 49(5), 854-866.
56. Ha, T. and Tinnefeld, P., 2012. Photophysics of fluorescent probes for single-molecule biophysics and super-resolution imaging. *Annual review of physical chemistry*, 63, 595-617.
57. Xie, X.S. and Trautman, J.K. Optical studies of single molecules at room temperature. *Annual review of physical chemistry*, **1998**, 49(1), 441-480.
58. Schlegel, G., Bohnenberger, J., Potapova, I. and Mews, A. Fluorescence decay time of single semiconductor nanocrystals. *Physical Review Letters*, **2003**, 88(13), p.137401.
59. Phillips, J.C. Stretched exponential relaxation in molecular and electronic glasses. *Reports on Progress in Physics*, **1996**, 59(9), 1133.
60. Clauset, A., Shalizi, C.R. and Newman, M.E. Power-law distributions in empirical data. *SIAM review*, **2009**, 51(4), 661-703.

CHAPTER 2: CONTRIBUTIONS FROM EXCITED-STATE PROTON AND ELECTRON TRANSFER TO THE BLINKING AND PHOTBLEACHING DYNAMICS OF ALIZARIN AND PURPURIN

Introduction

The fading of colors in works of art is a major challenge for the conservation of our cultural heritage.¹ As organic-based “fugitive” dyes and pigments fade upon exposure to light, the aesthetics of the composition as well as the original intention of the artist can be significantly altered.²⁻⁵ For example, red lake pigments such as madder lake, created by mixing natural, organic dyes with inorganic mordant salts to form insoluble pigments, were highly prized by artists for centuries despite their propensity to fade.⁴ Although madder lake is relatively colorfast compared to other red lakes, its light-induced fading is highly dependent on the molecular composition of the pigment. In particular, madder lake is primarily composed of alizarin (1,2-dihydroxyanthraquinone) and purpurin (1,2,4-trihydroxyanthraquinone), the main dyes extracted from madder root (*Rubia tinctorum* L.). Previous studies have shown that although alizarin-based pigments such as alizarin crimson are relatively photostable, madder lake pigments containing significant quantities of purpurin are highly susceptible to light-induced fading.^{3, 6-9} However, the mechanistic underpinnings of these observations are not well understood and are complicated by environmental heterogeneity. In the case of oil paintings, for example, chromophores are surrounded by an amalgamation of colorants, resins, gums, waxes, and oils, all of which deteriorate over multiple length- and time-scales. Elucidating the photophysical and photochemical foundations of fading is vital to our

understanding of material degradation, identifying early stages of deterioration, and formulating more-informed museum exhibition guidelines. Moreover, understanding the relative photostabilities of alizarin and purpurin are relevant to the design of inexpensive, earth-abundant dye-sensitized systems for solar-to-electrical and solar-to-fuel conversion.¹⁰⁻¹³

One strategy to decipher environmental heterogeneity is to employ single-molecule spectroscopy (SMS) methods. By virtue of its ability to probe the distributions of photophysical and photochemical behavior instead of just the ensemble-averaged values, SMS has been extensively applied to problems in photovoltaics,¹⁴⁻²¹ photocatalysis,²²⁻²³ and biology.²⁴⁻²⁵ Under continuous photoexcitation the emission from a single molecule is often intermittent, where emissive (on) and non-emissive (off) events are observed due to the population of optically bright and dark vibronic states such as the first excited singlet and triplet states, respectively.²⁶⁻³⁴ This so-called “blinking” is observed until the single-step photobleaching event, corresponding to irreversible conversion of a fluorophore to a non-emissive species. Therefore, single-molecule blinking measurements of the on-time, off-time, and photobleaching-time distributions can reveal the kinetics of dark-state population, depopulation, photobleaching, as well as the extent of kinetic dispersion. For example, previous single-molecule studies of synthetic, organic chromophores in polymers³⁵⁻³⁷ and on glass³⁸ have revealed complex photophysics (i.e., power-law distributions) as well as the dark states that serve as a gateway to photobleaching. However, single-molecule data that appear to follow power laws on log-log axes may not actually be power-law

distributed, a result that significantly changes the physical interpretation of blinking and photobleaching.^{14-15, 39-40}

In this study, the blinking and photobleaching processes of alizarin and purpurin on glass in N₂ are examined at the single-molecule level. We employ statistically-robust approaches based on change point detection (CPD),⁴¹ maximum likelihood estimate (MLE), Kolmogorov-Smirnov (KS) test, and log-likelihood ratio (LLR) test⁴² methods to analyze blinking dynamics and quantify the goodness-of-fit to various trial functions (i.e., power law, log-normal, Weibull) in order to determine the distribution that best represents the data. We find that the emissive and non-emissive event durations are best represented by log-normal and Weibull distributions, respectively. The observation of these distributions is consistent with complex excited-state photophysics and photochemistry involving: (1) a dispersive electron transfer (ET) pathway, in which the activation barrier for photoinduced ET from the molecules to glass is varied with time, and (2) an excited-state intramolecular proton transfer (ESIPT) process. Furthermore, we find that molecular photobleaching is preceded by ET. The combination of SMS measurements with robust statistical analysis and modeling reveals that despite striking structural similarity, the excited-state photochemistry of alizarin and purpurin is complex, distinct, and highly dependent on the kinetic competition between ET and ESIPT.

Experimental

Sample Preparation and Bulk Characterization

Alizarin (97%) and purpurin (95%) were used as received from Acros Organics. Solvents were used as received from Fisher Scientific. Deionized water (18.2 M Ω cm) was obtained using a water purification system (ThermoScientific, EasyPure II). Glass coverslips (Fisher Scientific, 12-545-102) were cleaned in a base bath for 24 hours, rinsed with deionized water, and dried using clean dry air (McMaster Carr, filter 5163K17). Solutions of alizarin and purpurin were prepared in ethanol and ethylacetate, respectively, and sonicated prior to sample preparation. For single-molecule measurements, 35 μ L of 10⁻⁹ M dye solution was deposited onto a clean cover slip using a spin coater (Laurell Technologies, WS-400-6NPP-LITE). The resulting samples were mounted in a custom designed flow cell for environmental control and flushed with dry N₂ throughout the experiments. Solution UV/vis and fluorescence measurements were performed on a Perkin Elmer Lambda 35 and Perkin Elmer LS-55 spectrophotometer, respectively.

Single-Molecule Microscopy and Data Analysis

Samples for single-molecule studies were placed in a custom-built flow cell atop a nanopositioning stage (Queensgate, NPS-XY-100B) and an inverted confocal microscope (Nikon, TiU). Laser excitation at 532 nm (Spectra Physics, Excelsior) was focused to a diffraction-limited spot using a high numerical aperture (NA) 100x oil-immersion objective (Nikon Plan Fluor, NA=1.3). Excitation powers (P_{exc}) of \sim 1 μ W and 5 μ W at the sample were used for single-

molecule measurements of alizarin and purpurin, respectively. Epifluorescence from the sample was collected through the objective, filtered (Semrock, LP03-532RS-2S), and focused onto an avalanche photodiode detector (APD) with a 50- μm aperture (MPD, PDM050CTB) to provide confocal resolution. A custom LabView program was used to control the nanopositioning stage in 100-nm steps and record emission counts. A z-axis microscope lock (Applied Science Instruments, MFC-2000) was used to maintain the focal plane of the objective during raster scans. Single-molecule resolution was established based on the observation of diffraction-limited spots, irreversible single-step photobleaching, and concentration dependence of the diffraction-limited spot density (i.e., ~ 10 molecules per $100 \mu\text{m}^2$). Blinking dynamics were acquired using a 10-ms integration time for ~ 100 s or until the single-step photobleaching event occurred.

Blinking dynamics were analyzed using the CPD method,⁴³ which reports statistically significant intensity change points as well as the number and temporal durations for up to 20 intensity levels. The durations of the first and last events were disregarded, since they are artificially set by the observation period. The lowest intensity level corresponds to a non-emissive (off) event or permanent photobleaching, depending on whether or not emission is recovered. Deconvolved states with intensities greater than one standard deviation above the rms noise (i.e., ~ 8 counts per 10 ms) are denoted as emissive (on). Consistent with previous studies,^{14-15, 40} the experimental on-event and off-event distributions are converted into complementary cumulative distribution functions (CCDFs) that describe the probability of an event occurring in a time greater than

or equal to t according to: $CCDF = 1 - \frac{1}{N} \sum_i t_i \leq t$. For clarity, we use the term probability distribution for CCDF throughout the paper. The fit parameters and corresponding goodness-of-fits of the experimental CCDFs relative to the proposed functional forms (i.e., power law, log-normal, Weibull) are quantified using MLE and the KS statistic (i.e., p value).^{14-15, 40, 42} Standard errors in the fit parameters are determined by calculating the inverse of the Hessian matrix (i.e., the second derivative of the log-likelihood with respect to the parameters). The log-likelihood ratio (LLR) and associated p-value ($p_{\mathcal{R}}$) are calculated according to the Vuong method.^{42, 44} Data analysis was performed in Matlab (version R2015b) with custom code.

Results and Discussion

Blinking Dynamics of Alizarin and Purpurin

A confocal microscope employing continuous 532-nm laser excitation was used to measure the time-dependent emission (i.e., blinking dynamics) of single alizarin and purpurin molecules on glass (Figure 1). Visual inspection of the blinking data in Figure 1 demonstrates that both single molecules exhibit multiple emissive intensities. Therefore, applying a simple threshold analysis to establish the temporal durations of emissive (on) or non-emissive (off) events is problematic. To address these issues, the single-molecule blinking dynamics of alizarin and purpurin were analyzed using the CPD method, which provides a more accurate determination of on and off events relative to thresholding.^{43, 45} The results of CPD analysis for the molecules in Figure 1 are overlaid on the blinking data and demonstrate that 16 and 14 deconvolved intensity levels are

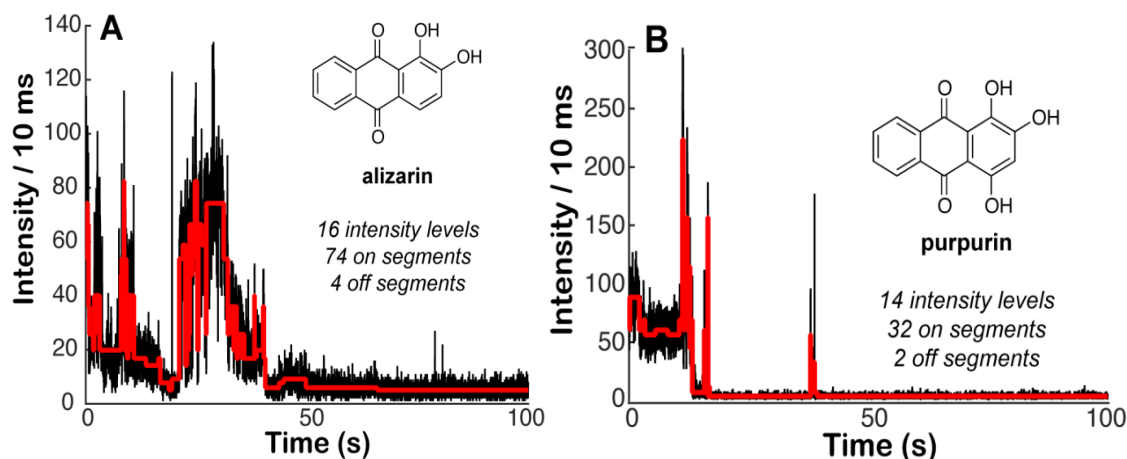


Figure 1. Representative single-molecule blinking dynamics of (A) alizarin and (B) purpurin on glass. The fluorescence intensity trajectory (black line) is recorded using continuous 532-nm laser excitation and a 10-ms integration time. Analysis of the blinking data with CPD demonstrates that 16 and 14 statistically-significant intensity levels are observed (red lines) for alizarin and purpurin, respectively.

observed for alizarin and purpurin, respectively. In addition to resolving multiple emission intensities, CPD also provides the ability to differentiate two types of events that are termed “segments” and “intervals”.⁴⁶

Segments correspond to the temporal duration of an event at a particular intensity. Intervals are then composed of successive segments. For example, on intervals correspond to the total duration of successive emissive segments that occur prior to an off event. The blinking trace of alizarin presented in Figure 1A exhibits 3 on intervals that are composed of 74 individual on segments as well as 3 off intervals that contain 3 off segments. The corresponding analysis for purpurin (Figure 1B) revealed a similar number of intensity levels, on intervals, and off intervals, but fewer than half the number of on segments (i.e., 32 for purpurin as compared to 74 for alizarin). The importance of differentiating between segments and intervals becomes more apparent for the blinking data

that is compiled from many molecules. In particular, the blinking dynamics of 137 alizarin molecules contained a total of 1830 on segments and 653 off segments. The corresponding analysis for 101 purpurin molecules yielded 403 on segments and 231 off segments. That is, the number of distinct emissive events per molecule is about four times higher for alizarin relative to purpurin. To examine the origin of this behavior, we investigated the possibility that multiple emissive intensities are observed due to the formation of an emissive phototautomer via excited-state intramolecular proton transfer (ESIPT). Previous studies have shown that upon photoexcitation of the normal 9,10-keto form (N) of alizarin, the molecule can undergo ESIPT to form the 1,10-keto tautomer (T). Since both forms are fluorescent (i.e., for alizarin in ethanol, fluorescence maxima at approximately 530 nm and 615 nm for N and T, solvent respectively, are observed),^{9, 47-48} the observation of dual emission that is dependent on solvent and excitation wavelength is a hallmark of ESIPT. Figure 2A shows the ensemble-averaged fluorescence spectra of 10^{-4} M alizarin in ethanol obtained using various excitation wavelengths (λ_{exc}). At λ_{exc} values greater than ~ 480 nm, a primary fluorescence peak centered at 524 nm is observed, consistent with emission from the locally-excited N state of alizarin. As excitation energy is increased to overcome the barrier to ESIPT, the emergence of another fluorescence band at 595 nm corresponding to the T is observed. Indeed, the ratio of N to T fluorescence (i.e., $N/T = I_{524}/I_{595}$ in ethanol) of alizarin in ethanol, acetonitrile, and chloroform solvents is increased at longer excitation wavelengths, consistent with ESIPT. Furthermore, dual emission is dependent,⁴⁹⁻

⁵⁰ with the most T emission observed in nonpolar solvents (Figure 2A, inset).

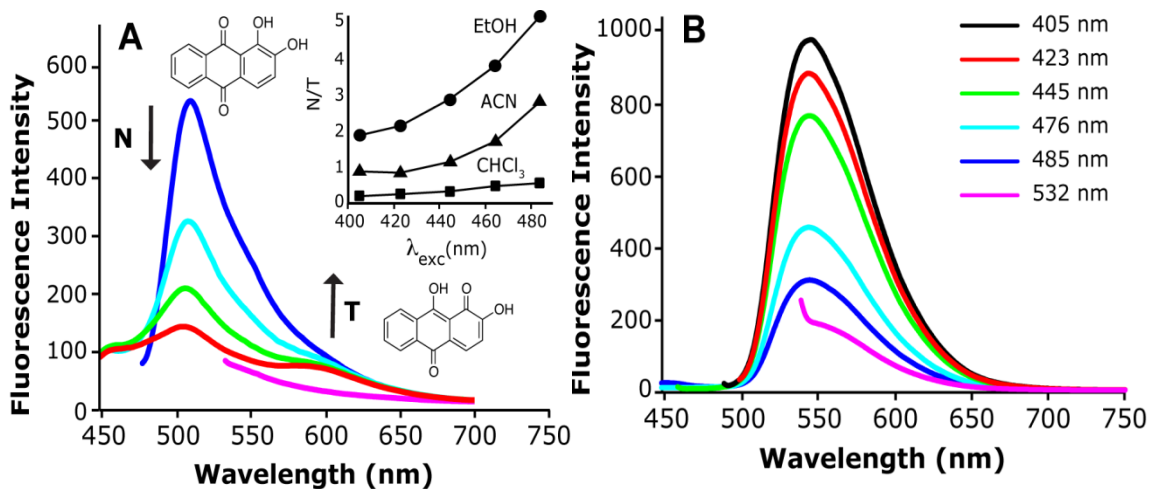


Figure 2. Ensemble-averaged fluorescence spectra of (A) 10^{-4} M alizarin in ethanol and (B) 10^{-5} M purpurin in acetonitrile. (black = 405 nm, red = 423 nm, green = 445 nm, cyan = 476 nm, blue = 485 nm, pink = 532 nm). (A) Two fluorescence maxima at 524 nm and 595 nm are observed corresponding to emission from the N and T forms of alizarin, respectively.⁴⁷ As excitation energy is increased, a concomitant increase in the relative fluorescence intensity (I_{fl}) of the phototautomer is observed. (inset) The ratio of N to T I_{fl} (i.e., $N/T = I_{524}/I_{595}$ in ethanol) of alizarin in ethanol, acetonitrile, and chloroform is increased at longer λ_{exc} , with the most T emission observed in $CHCl_3$. (B) In contrast, purpurin exhibits a single fluorescence maximum at 546 nm at all λ_{exc} .

The corresponding excitation-wavelength dependent fluorescence of purpurin in acetonitrile is presented in Figure 2B. The fluorescence spectra exhibit a single maximum at 546 nm, consistent with previous reports that hydroxyanthraquinones bearing a 1,4- substitution pattern do not undergo ES IPT.⁴⁸⁻⁵¹ In particular, according to nodal plane theory, purpurin has nodal planes that intersect and prevent stabilization of the 1,10-keto tautomer.⁵²⁻⁵³ Thus, the observation of more emissive segments for alizarin relative to purpurin is consistent with alizarin's ability to undergo ES IPT to form an emissive phototautomer. During single-molecule blinking measurements ES IPT is manifest as fluctuations in emission intensity as a result of different excited-state lifetimes

of the tautomers (i.e., 77 ps and 87 ps for N and T, respectively)^{47, 54} as well as the wavelength-dependent efficiency of the detector. The observation of multiple emissive intensities for purpurin may be evidence of a subpopulation of molecules that undergo ESIPT on glass, which would normally be hidden underneath the ensemble average.⁵⁵ However, we cannot rule out the possibility that spectral diffusion, time-dependent changes in the absorption spectrum of a molecule due to local environmental fluctuations, also plays a role in the observed emission dynamics.⁴⁵ Although fluctuations in emission intensity within an on interval can be attributed to ESIPT, it is unlikely that the production of an emissive phototautomer is responsible for the transition to a dark state. To determine the physical process responsible for blinking (i.e., switching between on and off events), the emissive and non-emissive intervals must be compiled and analyzed.

On- and Off-Interval Distributions

The blinking dynamics of ~100 molecules of alizarin and purpurin were compiled into on-interval and off-interval probability distributions (i.e., CCDFs) to extract the functional form and corresponding best-fit parameters. Figure 3 presents the resulting on-interval and off-interval probability distributions of 137 and 101 molecules of alizarin and purpurin, respectively. The on-interval distribution for alizarin contains 401 events, with individual values ranging from 0.02 to 94.1 s and an average on-interval duration of 6.62 s. The corresponding off-interval distribution consists of 392 events, with an average of 15.9 s and

individual values ranging from 0.08 to 89.81 s. The on- and off-interval distributions for purpurin are also peaked at short times, but exhibit different levels of dispersion relative to alizarin. Specifically, the on-interval distribution for purpurin contains 135 events, with individual values ranging from 0.04 to 36.58 s and an average duration of 3.71 s. The off-interval distribution for purpurin contains 158 events ranging from 0.06 to 94.09 s and an average duration of 26.01 s. Thus, purpurin exhibits a narrower on-interval distribution and broader off-interval distribution relative to alizarin. Furthermore, consistent with the aforementioned on-segment analysis, alizarin has an increased number of on intervals relative to purpurin.

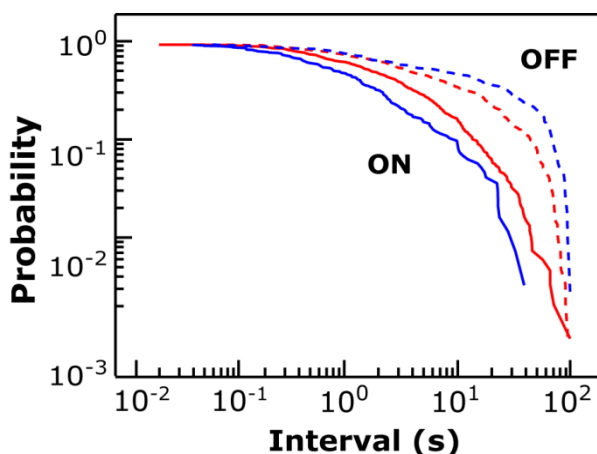


Figure 3. On- and off-interval probability distributions for alizarin and purpurin on glass. (red = alizarin, blue = purpurin, solid = on intervals, dashed = off intervals) The distributions of on intervals and off intervals are compiled from CPD analysis of the blinking dynamics of 137 and 101 molecules of alizarin and purpurin, respectively.

Identifying the functional forms of the on- and off-interval probability distributions is essential to elucidate the physical mechanism responsible for blinking. For example, although the on- and off-time distributions of rhodamines on TiO_2 were qualitatively fit by power laws, MLE/KS analysis revealed the data is actually log-normally distributed, consistent with the Albery model for ET (i.e.,

where the activation barriers are normally distributed).⁵⁶ Dispersive charge transport in disordered semiconductors has also been modeled using a continuous-time random walk model, which predicts population decays with a power-law form at long times and stretched-exponential form at short times (i.e., the Weibull distribution).⁵⁷⁻⁵⁹ To determine the physical mechanism for blinking in alizarin and purpurin, the on-interval and off-interval distributions were fit to power-law, log-normal, and Weibull test functions using a statistically robust MLE/KS approach described in detail elsewhere.^{14-15, 40} Briefly, a combination of MLE and KS tests are used to determine the best-fit parameters and the corresponding goodness-of-fit is determined using a KS test, which quantifies the distance between the empirical data and hypothesized model in a p-value. Here, the probability that the data matches the hypothetical model is increased as the p-value approaches unity and statistically-insignificant p-values ≤ 0.05 indicate that the model is not consistent with the data.^{40, 42}

Table 1 presents the best-fit parameters and corresponding p-values for power-law, log-normal, and Weibull fits to the on- and off-interval probability distributions for alizarin and purpurin. The fitting results presented in Table 1 demonstrate that the on intervals for alizarin and purpurin are well-represented by log-normal distributions, consistent with the observation of statistically-significant p-values (i.e., 0.07 and 0.67, respectively). The log-normal distribution occurs when the logarithm of the sample variable is normally distributed according to:

$$P(t) = \frac{1}{\sqrt{2\pi}\sigma t} e^{-\left[\frac{(\log(t)-\mu)^2}{2\sigma^2}\right]} \quad (1)$$

where the fit parameters μ and σ correspond to the geometric mean and standard deviation of the variable's natural logarithm, respectively. However, interpreting the MLE/KS analysis of the off-interval distributions is not as clear. According to the goodness-of-fit values, the power law is the only viable distribution to describe the off intervals. For example, the off-interval distribution for alizarin is best fit to a power law with $\alpha = 10.5 \pm 0.5$ and $p = 0.09$. However, previous studies have demonstrated the importance of quantifying the onset of power-law behavior (i.e., t_{min}) for analyzing the single-molecule on- and off-event distributions. In particular, MLE/KS analysis of the on- and off-event distributions for single rhodamine dyes on TiO_2 demonstrated that the power law is only operative for a small fraction of the data and that the log-normal distribution best represents the entire distribution.¹⁵ Attempts to fit the off-interval distributions of alizarin and purpurin to power laws generated exceedingly long t_{min} values of ~60 s (Table 1), meaning that just 5% and 20% of off intervals, respectively, are actually power-law distributed.

		Power Law: $\frac{\alpha-1}{t_{min}} \left(\frac{t}{t_{min}}\right)^{-\alpha}$			Log-normal: $\frac{1}{t\sigma\sqrt{2\pi}} e^{-\frac{(\ln(t)-\mu)^2}{2\sigma^2}}$			Weibull: $\frac{A}{B} \left(\frac{t}{B}\right)^{A-1} e^{-\left(\frac{t}{B}\right)^A}$		
		$t_{min}(s)$	α	p	μ	σ	p	A	B	p
ON	Alizarin	9.20	2.44 ± 0.07	0.04	0.81 ± 0.08	1.58 ± 0.06	0.07	0.68 ± 0.01	5.0 ± 0.4	0
	Purpurin	1.15	1.79 ± 0.07	0.05	0.1 ± 0.1	1.6 ± 0.1	0.67	0.63 ± 0.02	2.5 ± 0.3	0.02
OFF	Alizarin	65.73	10.5 ± 0.5	0.09	1.65 ± 0.09	1.74 ± 0.06	0	0.62 ± 0.01	12.0 ± 0.9	0
	Purpurin	57.38	5.2 ± 0.3	0.01	2.1 ± 0.2	2.0 ± 0.1	0	0.60 ± 0.01	25 ± 3	0

Table 1. Best-fit parameters and corresponding p-values for power-law, log-normal, and Weibull fits to the on- and off-interval probability distributions. Errors represent one standard deviation.

In cases where the p-values from KS tests are insufficient to make a firm distinction between hypotheses, the log-likelihood ratio (LLR) test provides the ability to directly compare two distributions against one another.⁴² Here, the logarithm of the ratio of the two likelihoods (\mathcal{R}) will be positive, negative, or zero depending on which distribution is better or in the event of a tie. In order to determine if specific values of \mathcal{R} are statistically significant (i.e., sufficiently far from zero), the standard deviation of \mathcal{R} must be considered by calculating a p-value ($p_{\mathcal{R}}$) according to the Vuong method.⁴⁴ If $p_{\mathcal{R}} < 0.1$, then the sign of \mathcal{R} is a reliable indicator of which model is the better fit to the data.

The results of the LLR tests for the on- and off-interval distributions of alizarin and purpurin are presented in Table 2. In all cases, the LLR tests provide the ability to differentiate between the distributions, consistent with calculated $p_{\mathcal{R}}$ values that are all close to zero. For completeness, we first tested the power-law distribution as the null hypothesis against log-normal and Weibull functions for both on and off intervals. The previous KS tests revealed that a power law poorly represents the on-interval distribution of alizarin (i.e., $p = 0.04$). Indeed, when the power law is tested against the log-normal and Weibull distributions, the resulting negative \mathcal{R} values indicate that either distribution is a better alternative to the power law. When the log-normal distribution is then tested against the Weibull distribution, the null (log-normal) distribution cannot be rejected, consistent with a large positive \mathcal{R} value (e.g., $\mathcal{R} = 1793.16$ for alizarin on intervals). Thus, KS and LLR tests are in agreement that on intervals are log-normally distributed.

		Power Law	Log-normal		Weibull		Log-normal	Weibull	
		p	\mathcal{R}	$p_{\mathcal{R}}$	\mathcal{R}	$p_{\mathcal{R}}$	p	\mathcal{R}	$p_{\mathcal{R}}$
ON	Alizarin	0.04	-120.98	0	-127.34	0	0.07	1793.16	0
	Purpurin	0.05	-106.00	0	-111.90	0	0.67	654.02	0
OFF	Alizarin	0.09	-7.83	~0	-8.16	~0	0	-28.17	~0
	Purpurin	0.01	-50.98	0	-53.85	0	0	-397.21	0

Table 2. p -values for fits to the null distribution as well as \mathcal{R} and $p_{\mathcal{R}}$ values for the alternatives.

Whereas the KS test is sufficient to establish the best fit to the on-interval distributions of alizarin and purpurin, the corresponding analysis of the off-interval distributions were inconclusive. Therefore, to determine if one distribution is preferred, we employed LLR tests with the log-normal distribution set as the null that is tested against the Weibull distribution. Table 2 demonstrates that the off-interval distributions are better described by the Weibull distribution, consistent with the observation of negative \mathcal{R} values of -28.17 and -397.21 for alizarin and purpurin, respectively. These findings are consistent with the observation that the off-segment probability distributions of alizarin and purpurin are best fit to Weibull distributions. Ultimately, the combination of MLE/KS and LLR tests provides the ability to determine the function that best represents the on- and off-interval probability distributions for alizarin and purpurin. These results also illustrate the utility of LLR tests in cases where the p-value alone is insufficient to determine the best fit between the empirical data and hypothesized model.

Analyzing the blinking dynamics of alizarin and purpurin on glass using CPD, MLE/KS, and LLR tests demonstrates that on intervals are log-normally distributed and off intervals are Weibull distributed (Tables 1 and 2). Our previous studies of individual rhodamine molecules on TiO_2 demonstrated that the observation of log-normal distributions is consistent with a dispersive ET kinetics model for blinking.¹⁴⁻¹⁵ In particular, Monte Carlo simulations based on the Albery model for heterogeneous ET, which assumes a Gaussian distribution of activation energies,⁵⁶ successfully reproduced the experimentally observed on- and off-event distributions. Therefore, the observation of log-normal distributions

for alizarin and purpurin on glass is consistent with the Albery model for ET. In this context, the electron injection process that occurs from the dye to glass is dispersive due to local variations in the activation energy (e.g., with binding site, trap state energy and distance). However, the Albery model predicts that both the on- and off-event distributions are log-normally distributed and we find that off intervals are better described by Weibull distributions. The Weibull distribution occurs when a fractional power law is inserted into a stretched exponential function:

$$\frac{A}{B} \left(\frac{t}{B}\right)^{A-1} e^{-\left(\frac{t}{B}\right)^A} \quad (2)$$

where A is the shape parameter and B is the scale parameter. Like the log-normal distribution, the Weibull function accounts for dispersive charge transfer kinetics using a superposition of first-order decay functions that originate from an asymmetric Gaussian distribution of energies.^{40, 58, 60-62} For example, Azechi and co-workers recently demonstrated that perylenediimide dyes in a disordered polymer matrix exhibit on-event distributions that are best represented by Weibull distributions, owing to radical ion pair intersystem crossing via charge hopping between trap sites in the polymer.⁶¹ Therefore, the observation of log-normal and Weibull distributions indicates that the blinking (i.e., switching between on and off events) of alizarin and purpurin is due to dispersive ET kinetics involving Gaussian-like distributions of activation energies. Ultimately, we find that transitions between emissive states are due to ESIPT and switching between emissive and non-emissive states originates from dispersive ET. To investigate the impact of these photophysical and photochemical transformations on

molecular photobleaching, we examined the intensities and durations of the last event that precedes photobleaching.

Role of ESIPT and ET in Single-Molecule Photobleaching

Blinking measurements can also probe single-molecule photobleaching, which corresponds to a photo-induced reaction to yield a non-fluorescent product. Indeed, previous blinking studies of a perylene trimer demonstrated that electron tunneling to a non-emissive radical cation state leads to photodegradation, since long-lived dark states were observed to precede the single-step photobleaching event.³⁶ To determine the role of ESIPT and ET in the photobleaching of alizarin and purpurin, we investigated the intensities and durations of the last event that precedes photobleaching. Of the ~100 single-molecule blinking traces of alizarin and purpurin that were measured and analyzed using CPD, 64 (47%) and 37 (37%), respectively, exhibited single-step photobleaching within the measurement window.

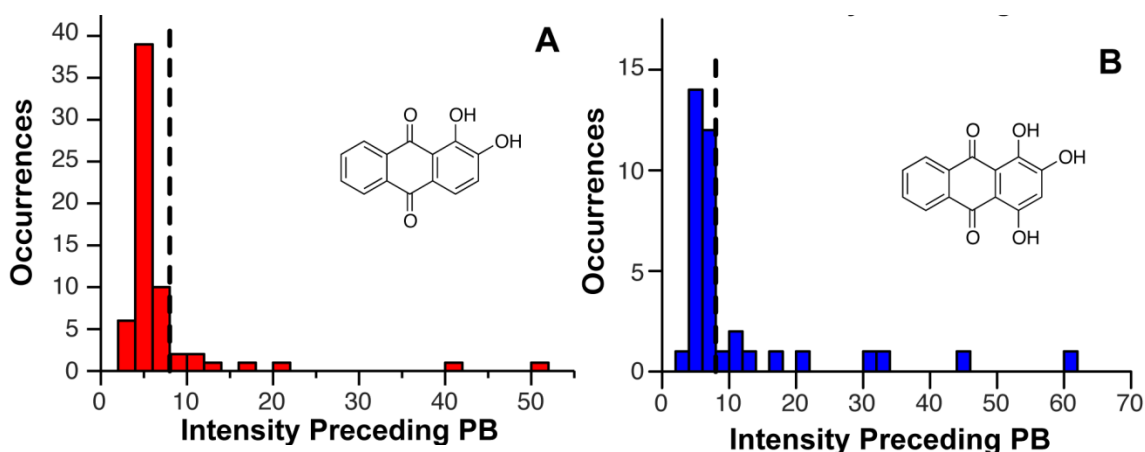


Figure 4. Intensity distributions for the last event before photobleaching (PB) for: (A) 64 single molecules of alizarin, and (B) 37 single molecules of purpurin. Average intensities were 7 ± 1 and 5 ± 2 counts per 10 ms for alizarin and purpurin, respectively, where the error corresponds to the standard deviation of the mean. Dashed lines correspond to the average threshold (i.e., ~8 counts per 10 ms) that was used to differentiate emissive and non-emissive events using CPD.

Figure 4 presents histograms of the intensities corresponding to the last event before photobleaching for these molecules. The intensity distribution for alizarin contains individual values ranging from 3 to 52 counts per 10 ms and an average intensity of 7 ± 1 counts per 10 ms, with the error corresponding to the standard deviation of the mean. The corresponding intensity distribution for purpurin is also peaked at low intensities, with an intensity of 11 ± 2 counts per 10 ms and individual values ranging from 4 to 60 counts per 10 ms. Since states with intensities less than one standard deviation above the rms noise (i.e., <8 counts per 10 ms) are considered to be non-emissive, the vast majority of events preceding photobleaching (i.e., 86% and 73% for alizarin and purpurin, respectively) are dark. That is, photobleaching is most often preceded by an ET event to populate a non-emissive radical cation state.

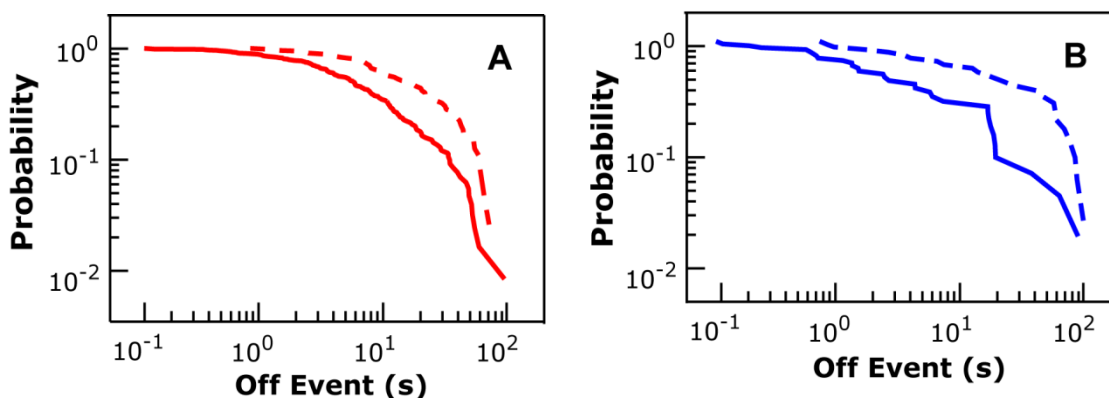


Figure 5. Off-event probability distributions derived from CPD analysis for (A) alizarin (B) purpurin. The durations of the off events that precede photobleaching (dashed lines) are markedly longer relative to the durations of all other off events recorded during blinking (solid lines). For 64 single molecules of alizarin, the average duration of the off event that precedes photobleaching (i.e., 20 ± 2 s) is approximately double the average duration for all other off events (i.e., 10 ± 2 s). Corresponding average off-event durations for 37 single molecules of purpurin are 29 ± 5 s and 8 ± 2 s, respectively.

Further evidence of this interpretation is provided by the off-event probability distributions presented in Figure 5, which compares the durations of

the off events preceding photobleaching to the durations of all other off events recorded during blinking. In all cases, broad off-event distributions are observed, consistent with dispersive charge recombination. Furthermore, the durations of the off events that lead to photobleaching are markedly longer relative to the durations of all other off events. For 64 single molecules of alizarin, the average duration of the off event that precedes photobleaching (i.e., 20 ± 2 s) is approximately double the average duration of all other off events (i.e., 10 ± 2 s). The corresponding average off-event durations for 37 single molecules of purpurin are 29 ± 5 s and 8 ± 2 s, respectively. These observations are consistent with the interpretation that the longer alizarin and purpurin reside in the dark ET state, the more likely they are to photobleach.

These results are summarized in a proposed mechanism for the blinking and photobleaching of alizarin and purpurin (Figure 6). Upon photoexcitation of the lowest-energy ground state of alizarin (N),⁴⁹ the locally-excited state (N*) is populated. Depending on the excitation wavelength and local environment, alizarin can emit or undergo ES IPT to populate the excited T state (T*), which returns to the lowest-energy ground state through emission and subsequent ground-state proton transfer (PT). Alternatively, N* can decay through dispersive electron injection to glass to populate a non-emissive radical cation state that is followed by repopulation of N through dispersive back ET (BET). Otherwise, the formation of the radical cation state leads to permanent photobleaching. Thus, the photobleaching of alizarin is dependent on the competition between excited-state ET and ES IPT pathways. In contrast, the photophysics of purpurin can be

described by a relatively simple three-level system, whereupon excitation of the molecule to the singlet-excited state (N^*) can result in dispersive electron injection to form the non-emissive radical cation state. If the purpurin radical cation does not undergo BET to repopulate the ground state, then the photobleaching event occurs. Therefore, in the absence of the ESIPT pathway, the photobleaching of purpurin is solely dependent on the ET dynamics of the system.

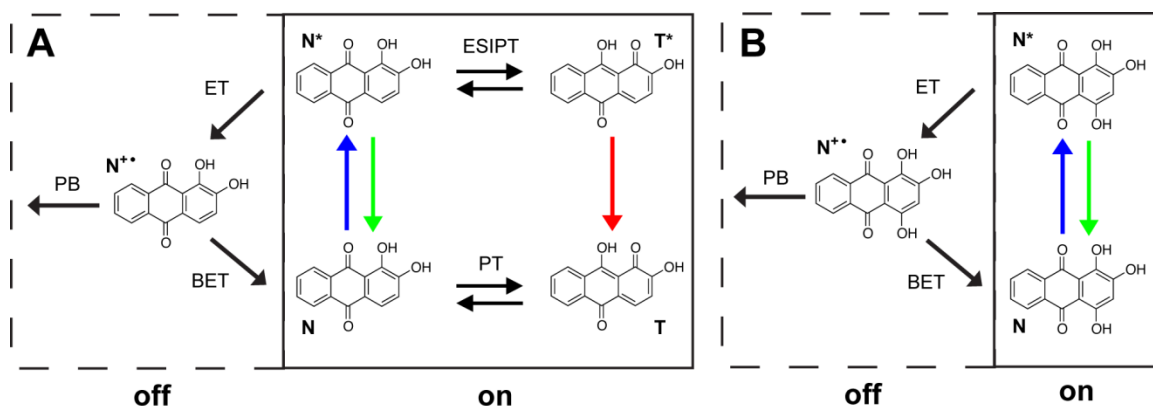


Figure 6. Proposed mechanism for the blinking and photobleaching of (A) alizarin and (B) purpurin on glass.

The best-fit parameters of the on- and off-interval distributions reveal further insights on the relative photostabilities of alizarin and purpurin. A previous study demonstrated the relationship between the experimentally observed log-normal fit parameters and the underlying ET kinetics.¹⁵ In short, $-\mu_{on}$ is proportional to the average rate constant for injection (i.e., $-\mu_{on} = \langle \ln(k_{on}) \rangle$), and σ_{on} is proportional to the energetic dispersion around the mean activation barrier. Therefore, the best-fit parameters for the on-interval distributions in Table 1 demonstrate that alizarin has a slower average injection rate relative to purpurin (i.e., $-\mu_{on} = -0.81 \pm 0.08$ for alizarin and $-\mu_{on} = -0.1 \pm 0.1$ for purpurin). The

energetic dispersion is approximately equal for both molecules (i.e., $\sigma_{on} \sim 1.6$). The fit parameters of the off-interval Weibull distributions also reveal information about the underlying ET kinetics. The shape parameter, A, shows the extent of “statistical aging”, where $A < 1$ mean that the probability of a molecule leaving a particular state is decreased over time.⁴⁰ MLE/KS analysis demonstrates that the off-interval distributions for alizarin and purpurin exhibit A values less than 1 (i.e., 0.62 ± 0.01 and 0.60 ± 0.01 , respectively). Therefore, the probability of dark-state depopulation through BET is decreased with time. This result is consistent with the data presented in Figure 5, which demonstrate that long-lived dark states lead to photobleaching. Finally, taking into account both the A and B fit parameters of the off-interval distributions (i.e., $B = 12.0 \pm 0.9$ for alizarin and $B = 25 \pm 3$ for purpurin), we find that the average off-interval duration is longer for purpurin relative to alizarin. That is, purpurin exhibits a slower average BET rate as compared to alizarin. Altogether, these results explain the observed differences in the ensemble-averaged fading of alizarin and purpurin in the context of relative contributions from ESIPT and ET. The ability of alizarin to undergo ESIPT enables fast excited-state decay and decreases unwanted ET. In contrast, purpurin exhibits faster ET and slower BET relative to alizarin, leading to increased photobleaching via the dark ET state.

Conclusion

Previous studies have shown that although alizarin is relatively photostable, purpurin is susceptible to rapid light-induced fading.^{3, 6-9} Our single-

molecule studies of alizarin and purpurin on glass reveal new insights about the mechanistic underpinnings of these observations. The number of distinct emissive events per molecule is about four times higher for alizarin relative to purpurin, consistent with alizarin's ability to undergo ESIPT to populate an emissive tautomer state. Although ESIPT can explain differences in emissive events between alizarin and purpurin, to determine the process responsible for blinking (i.e., switching between on and off events), the on- and off-interval distributions were fit to various test functions using MLE/KS and LLR tests. We determined that the on- and off-interval distributions are best represented by log-normal and Weibull distributions, respectively, consistent with a dispersive ET model for blinking. To understand the role of ESIPT and ET in the photobleaching of alizarin and purpurin, we examined the intensities and durations of the last event preceding photobleaching. By analyzing the single-molecule blinking traces with the robust CPD method, we find that photobleaching is most often preceded by an ET event. Furthermore, the longer alizarin and purpurin reside in the dark radical cation state, the more likely they are to photobleach. Thus, the relative photostabilities of alizarin and purpurin are best understood in the context of kinetic competition between a dispersive ET pathway, in which the activation free energy for photoinduced ET from the molecules to glass is varied with time, and ESIPT. Altogether, our single-molecule blinking and photobleaching study of alizarin and purpurin reveal why two chromophores with striking structural similarity exhibit drastically different fading properties.

Acknowledgements

Acknowledgement is made to the Research Corporation (MI-CSSA #22491) for support of this research. We thank the NASA Virginia Space Grant Consortium for support of this project through a Graduate Research Fellowship to J.A.T. The Charles Center at William and Mary provided summer funding for J.A.T., K.A.T., and A.F.O. We thank Brian Howerton (Aero Solutions Consulting) for design and implementation of the custom Labview program to collect blinking dynamics. This work was performed in part using computational facilities at William and Mary, which were provided with the assistance of the National Science Foundation, the Virginia Port Authority, Sun Microsystems, and Virginia's Commonwealth Technology Research Fund. We thank Eric J. Walter for assistance with computations on the SciClone cluster and Tolga Karsili (University of Bristol) for helpful discussions about the excited-state trajectories of alizarin and purpurin.

References

1. Schaeffer, T. T., *Effects of Light on Materials in Collections: Data on Photoflash and Related Sources*; Getty Publications: Los Angeles, CA, 2001.
2. Kirby, J.; Spring, M.; Higgit, C., The Technology of Eighteenth- and Nineteenth-Century Red Lake Pigments. *Nat. Gall. Tech. Bull.* **2007**, 28, 69-95.
3. Saunders, D.; Kirby, J., Light-Induced Colour Changes in Red and Yellow Lake Pigments. *Nat. Gall. Tech. Bull.* **1994**, 79-97.
4. Talley, M. K., All Good Pictures Crack. In Reynolds, Penny, N., Ed. *Royal Academy of Arts*: 1986; p 65.
5. van Eikema Hommes, M., *Changing Pictures: Discoloration in 15th-17th-Century Oil Paintings*; Archetype Publications Ltd.: London, 2004.
6. Padfield, T.; Landi, S., The Light-Fastness of the Natural Dyes. *Studies in Conservation* **1966**, 11, 181-196.
7. Clementi, C.; Nowik, W.; Romani, A.; Cibir, F.; Favaro, G., A Spectrometric and Chromatographic Approach to the Study of Ageing of Madder (*Rubia Tinctorum* L.) Dyestuff on Wool. *Anal. Chim. Acta* **2007**, 596, 46-54.
8. Cristea, D.; Vilarem, G., Improving Light Fastness of Natural Dyes on Cotton Yarn. *Dyes Pigments* **2006**, 70, 238-245.
9. Grazia, C.; Clementi, C.; Miliani, C.; Romani, A., Photophysical Properties of Alizarin and Purpurin Al(III) Complexes in Solution and in Solid State. *Photochem. Photobiol. Sci.* **2011**, 10, 1249-1254.
10. Duncan, W. R.; Prezhdo, O. V., Theoretical Studies of Photoinduced Electron Transfer in Dye-Sensitized TiO₂. *Annu. Rev. Phys. Chem.* **2007**, 58, 143-184.
11. Duncan, W. R.; Stier, W. M.; Prezhdo, O. V., Ab Initio Nonadiabatic Molecular Dynamics of the Ultrafast Electron Injection across the Alizarin/TiO₂ Interface. *J. Amer. Chem. Soc.* **2005**, 127, 7941-7951.
12. Cecconi, B.; Manfredi, N.; Montini, T.; Fornasiero, P.; Abbotto, A., Dye-Sensitized Solar Hydrogen Production: The Emerging Role of Metal-Free Organic Sensitizers. *Eur. J. Org. Chem.* **2016**, 10.1002/ejoc.201600653.
13. Willkomm, J.; Orchard, K. L.; Reynal, A.; Pastor, E.; Durrant, J. R.; Reisner, E., Dye-Sensitized Semiconductors Modified with Molecular Catalysts for Light-Driven H₂ Production. *Chem. Soc. Rev.* **2016**, 45, 9-23.
14. Wong, N. Z.; Ogata, A. F.; Wustholz, K. L., Dispersive Electron-Transfer Kinetics from Single Molecules on TiO₂ Nanoparticle Films. *J. Phys. Chem. C* **2013**, 117, 21075-21085.
15. Tan, J. A.; Rose, J. T.; Cassidy, J. P.; Rohatgi, S. K.; Wustholz, K. L., Dispersive Electron-Transfer Kinetics of Rhodamines on TiO₂: Impact of Structure and Driving Force on Single-Molecule Photophysics. *J. Phys. Chem. C* **2016**, 10.1021/acs.jpcc.6b01960.
16. Govind Rao, V.; Dhital, B.; Lu, H. P., Probing Driving Force and Electron Accepting State Density Dependent Interfacial Electron Transfer Dynamics: Suppressed Fluorescence Blinking of Single Molecules on Indium Tin Oxide Semiconductor. *J. Phys. Chem. B* **2016**.
17. Govind Rao, V.; Lu, H. P., Inhomogeneous and Complex Interfacial Electron Transfer Dynamics: A Single-Molecule Perspective. *ACS Energy Lett.* **2016**.
18. Govind Rao, V.; Dhital, B.; He, Y.; Lu, H. P., Single-Molecule Interfacial Electron Transfer Dynamics of Porphyrin on TiO₂ Nanoparticles: Dissecting the Complex Electronic Coupling Dependent Dynamics. *J. Phys. Chem. C* **2014**, 118, 20209-20221.
19. Sevinc, P. C.; Wang, X.; Wang, Y. M.; Zhang, D.; Meixner, A. J.; Lu, H. P., Simultaneous Spectroscopic and Topographic near-Field Imaging of TiO₂ Single Surface States and Interfacial Electronic Coupling. *Nano Lett.* **2011**, 11, 1490-1494.
20. Guo, L.; Wang, Y.; Lu, H. P., Combined Single-Molecule Photon-Stamping Spectroscopy and Femtosecond Transient Absorption Spectroscopy Studies of Interfacial Electron Transfer Dynamics. *J. Amer. Chem. Soc.* **2010**, 132, 1999-2004.
21. Wang, Y. M.; Wang, X. F.; Lu, H. P., Probing Single-Molecule Interfacial Geminate Electron-Cation Recombination Dynamics. *J. Amer. Chem. Soc.* **2009**, 131, 9020-9025.

22. Sambur, J. B.; Chen, P., Distinguishing Direct and Indirect Photoelectrocatalytic Oxidation Mechanisms Using Quantitative Single-Molecule Reaction Imaging and Photocurrent Measurements. *J. Phys. Chem. C* **2016**.
23. Tachikawa, T.; Yamashita, S.; Majima, T., Evidence for Crystal-Face-Dependent TiO₂ Photocatalysis from Single-Molecule Imaging and Kinetic Analysis. *J. Amer. Chem. Soc.* **2011**, 133, 7197-7204.
24. Pertsinidis, A.; Zhang, Y.; Chu, S., Subnanometre Single-Molecule Localization, Registration and Distance Measurements. *Nature* **2010**, 466, 647-651.
25. Milenkovic, L.; Weiss, L. E.; Yoon, J.; Roth, T. L.; Su, Y. S.; Sahl, S. J.; Scott, M. P.; Moerner, W. E., Single-Molecule Imaging of Hedgehog Pathway Protein Smoothed in Primary Cilia Reveals Binding Events Regulated by Patched1. *Proc. Nat. Acad. Sci.* **2015**, 112, 8320-8325.
26. Bernard, J.; Fleury, L.; Talon, H.; Orrit, M., Photon Bunching in the Fluorescence from Single Molecules - a Probe for Intersystem Crossing. *J. Chem. Phys.* **1993**, 98, 850-859.
27. Basche, T.; Kummer, S.; Brauchle, C., Direct Spectroscopic Observation of Quantum Jumps of a Single-Molecule. *Nature* **1995**, 373, 132-134.
28. Kulzer, F.; Kummer, S.; Basche, T.; Brauchle, C., Quantum Jumps of Single Molecules: A Method to Measure Triplet Kinetics. *J. Infor. Rec.* **1996**, 22, 567-572.
29. Ha, T.; Enderle, T.; Chemla, D. S.; Selvin, P. R.; Weiss, S., Quantum Jumps of Single Molecules at Room Temperature. *Chem. Phys. Lett.* **1997**, 271, 1-5.
30. Walla, P. J.; Jelezko, F.; Tamarat, P.; Lounis, B.; Orrit, M., Perylene in Biphenyl and Anthracene Crystals: An Example of the Influence of the Host on Single-Molecule Signals. *Chem. Phys.* **1998**, 233, 117-125.
31. Yip, W. T.; Hu, D. H.; Yu, J.; Vanden Bout, D. A.; Barbara, P. F., Classifying the Photophysical Dynamics of Single- and Multiple-Chromophoric Molecules by Single Molecule Spectroscopy. *J. Phys. Chem. A.* **1998**, 102, 7564-7575.
32. Veerman, J. A.; Garcia-Parajo, M. F.; Kuipers, L.; van Hulst, N. F., Time-Varying Triplet State Lifetimes of Single Molecules. *Phys. Rev. Lett.* **1999**, 83, 2155-2158.
33. Weston, K. D.; Carson, P. J.; DeAro, J. A.; Buratto, S. K., Single-Molecule Detection Fluorescence of Surface-Bound Species in Vacuum. *Chem. Phys. Lett.* **1999**, 308, 58-64.
34. Vosch, T., et al., Influence of Structural and Rotational Isomerism on the Triplet Blinking of Individual Dendrimer Molecules. *Angew. Chem., Int. Ed. Engl.* **2001**, 40, 4643-+.
35. Renn, A.; Seelig, J.; Sandoghdar, V., Oxygen-Dependent Photochemistry of Fluorescent Dyes Studied at the Single Molecule Level. *Mol. Phys.* **2006**, 104, 409-414.
36. Hoogenboom, J. P.; van Dijk, E.; Hernando, J.; van Hulst, N. F.; Garcia-Parajo, M. F., Power-Law-Distributed Dark States Are the Main Pathway for Photobleaching of Single Organic Molecules. *Phys. Rev. Lett.* **2005**, 95, 097401.
37. Zondervan, R.; Kulzer, F.; Kol'chenk, M. A.; Orrit, M., Photobleaching of Rhodamine 6g in Poly(Vinyl Alcohol) at the Ensemble and Single-Molecule Levels. *J. Phys. Chem. A.* **2004**, 108, 1657-1665.
38. Yeow, E. K. L.; Melnikov, S. M.; Bell, T. D. M.; De Schryver, F. C.; Hofkens, J., Characterizing the Fluorescence Intermittency and Photobleaching Kinetics of Dye Molecules Immobilized on a Glass Surface. *J. Phys. Chem. A.* **2006**, 110, 1726-1734.
39. Riley, E. A.; Hess, C. M.; Pioquinto, J. R. L.; Kaminsky, W.; Kahr, B.; Reid, P. J., Proton Transfer and Photoluminescence Intermittency of Single Emitters in Dyed Crystals. *J. Phys. Chem. B* **2013**, 117, 4313-4324.
40. Riley, E. A.; Hess, C. M.; Whitham, P. J.; Reid, P. J., Beyond Power Laws: A New Approach for Analyzing Single Molecule Photoluminescence Intermittency. *J. Chem. Phys.* **2012**, 136, 10.
41. Zhang, K.; Chang, H.; Fu, A.; Alivisatos, A. P.; Yang, H., Continuous Distribution of Emission States from Single Cdse/Zns Quantum Dots. *Nano Lett.* **2006**, 6, 843-847.
42. Clauset, A.; Shalizi, C.; Newman, M., Power-Law Distributions in Empirical Data. *Siam Rev.* **2009**, 51, 661-703.
43. Watkins, L. P.; Yang, H., Detection of Intensity Change Points in Time-Resolved Single-Molecule Measurements. *J. Phys. Chem. B* **2005**, 109, 617-628.
44. Vuong, Q. H., Likelihood Ratio Tests for Model Selection and Non-Nested Hypotheses. *Econometrica* **1989**, 57, 307-333.

45. Wustholz, K. L.; Bott, E. D.; Kahr, B.; Reid, P. J., Memory and Spectral Diffusion in Single-Molecule Emission. *J. Phys. Chem. C* **2008**, 112, 7877-7885.
46. Riley, E. A.; Bingham, C.; Bott, E. D.; Kahr, B.; Reid, P. J., Two Mechanisms for Fluorescence Intermittency of Single Violamine R Molecules. *Phys. Chem. Chem. Phys.* **2011**, 13, 1879-1887.
47. Lee, S.; Lee, J.; Pang, Y., Excited State Intramolecular Proton Transfer of 1,2-Dihydroxyanthraquinone by Femtosecond Transient Absorption Spectroscopy. *Curr. Appl. Phys.* **2015**, 15, 1492-1499.
48. Miliani, C.; Romani, A.; Favaro, G., Acidichromic Effects in 1,2-Di- and 1,2,4-Trihydroxyanthraquinones. A Spectrophotometric and Fluorimetric Study. *J. Phys. Org. Chem.* **2000**, 13, 141-150.
49. Amat, A.; Miliani, C.; Romani, A.; Fantacci, S., Dft/Tddft Investigation on the Uv-Vis Absorption and Fluorescence Properties of Alizarin Dye. *Phys. Chem. Chem. Phys.* **2015**, 17, 6374-6382.
50. Claro, A.; Melo, M. J.; Schafer, S.; de Melo, J. S. S.; Pina, F.; van den Berg, K. J.; Burnstock, A., The Use of Microspectrofluorimetry for the Characterization of Lake Pigments. *Talanta* **2008**, 74, 922-929.
51. Carter, T. P.; Gillispie, G. D.; Connoll, M. A., Intramolecular Hydrogen Bonding in Substituted Anthraquinones by Laser-Induced Fluorescence. 1. 1,4-Dihydroxyanthraquinone (Quinizarin). *J. Phys. Chem.* **1982**, 86, 192-196.
52. Nagaoka, S.-i.; Nagashima, U., Effects of Node of Wave Function Upon Excited-State Intramolecular Proton Transfer of Hydroxyanthraquinones and Aminoanthraquinones. *Chem. Phys.* **1996**, 206, 353-362.
53. Nagaoka, S.; Nagashima, U., Effects of Nodal Plane of Wave Function Upon Photochemical Reactions of Organic Molecules. *J. Phys. Chem.* **1990**, 94, 1425-1431.
54. Matylitsky, V. V.; Lenz, M. O.; Wachtveitl, J., Observation of Ph-Dependent Back-Electron-Transfer Dynamics in Alizarin/Tio₂ Adsorbates: Importance of Trap States. *J. Phys. Chem. B* **2006**, 110, 8372-8379.
55. Moerner, W. E.; Fromm, D. P., Methods of Single-Molecule Fluorescence Spectroscopy and Microscopy. *Rev. Sci. Instrum.* **2003**, 74, 3597-3619.
56. Albery, W. J.; Bartlett, P. N.; Wilde, C. P.; Darwent, J. R., A General-Model for Dispersed Kinetics in Heterogeneous Systems. *J. Amer. Chem. Soc.* **1985**, 107, 1854-1858.
57. Nelson, J.; Chandler, R. E., Random Walk Models of Charge Transfer and Transport in Dye Sensitized Systems. *Coord. Chem. Rev.* **2004**, 248, 1181.
58. Nelson, J.; Haque, S. A.; Klug, D. R.; Durrant, J. R., Trap-Limited Recombination in Dye-Sensitized Nanocrystalline Metal Oxide Electrodes. *Phys. Rev. B* **2001**, 63.
59. Nelson, J., Continuous-Time Random-Walk Model of Electron Transport in Nanocrystalline Tio₂ Electrodes. *Phys. Rev. B* **1999**, 59, 15374-15380.
60. McNeil, I. J.; Ashford, D. L.; Luo, H. L.; Fecko, C. J., Power-Law Kinetics in the Photoluminescence of Dye-Sensitized Nanoparticle Films: Implications for Electron Injection and Charge Transport. *J. Phys. Chem. C* **2012**, 116, 15888-15899.
61. Mitsui, M.; Unno, A.; Azechi, S., Understanding Photoinduced Charge Transfer Dynamics of Single Perylenediimide Dyes in a Polymer Matrix by Bin-Time Dependence of Their Fluorescence Blinking Statistics. *J. Phys. Chem. C* **2016**, 120, 15070-15081.
62. Nelson, J.; Chandler, R. E., Random Walk Models of Charge Transfer and Transport in Dye Sensitized Systems. *Coord. Chem. Rev.* **2004**, 248, 1181-1194.

APPENDIX I: FLUORESCENCE BLINKING AS AN OUTPUT SIGNAL FOR PROGRAMMABLE BIOSENSING

Introduction

In recent years, the field of biosensing has been introduced to colloidal luminescent semiconductor nanoparticles, better known as quantum dots (QDs)¹⁻⁹. QDs are composed of a semiconducting core and a shell that protects against oxidation¹⁰. Their size-tunable optical properties, due to quantum confinement, yield narrow, wavelength specific emission spectra while maintaining a broad excitation range, resulting in polychromic fluorescence with a relatively uniform excitation energy. QDs offer a better shelf life and a higher resistance to photodegradation compared to small organic dyes and their high surface area is amenable to a wide range of chemical modifications^{7,11-13}. These properties make them attractive for biosensing applications¹⁴ and have led to the development of inexpensive, sensitive, and multiplexed assays¹⁵, e.g., the detection of oncogenic mRNAs using QD DNA conjugates^{16,17}.

To date, all QD-based biosensing approaches have required a change in fluorescence intensity or color to confirm the presence or absence of a biomolecule^{18,19}. For this to occur, QDs must be engineered with a local coordination environment that, after selective interaction with an analyte, is able to undergo an electron or energy transfer reaction with the QD. The signal from this type of sensor is usually straightforward to detect, but it is not always convenient to design a QD system that can undergo such dramatic fluorescence

changes, which are inherently sensitive to donor-acceptor distances and small changes in the local environment.

Here, we propose a more robust sensing strategy, which eliminates the need for any analyte-induced changes in the fluorescence from individual particles. Instead, QDs are programmed to aggregate after interaction with a target molecule, and fluorescence differences between QD aggregates and monomers are used to report their detection. The proposed method relies on an intrinsic property of most QDs and many other chromophores known as fluorescence blinking. Single QDs typically exhibit binary fluorescence blinking trajectories (Figure 1) that alternate between bright (on) and dark (off) states,²⁰

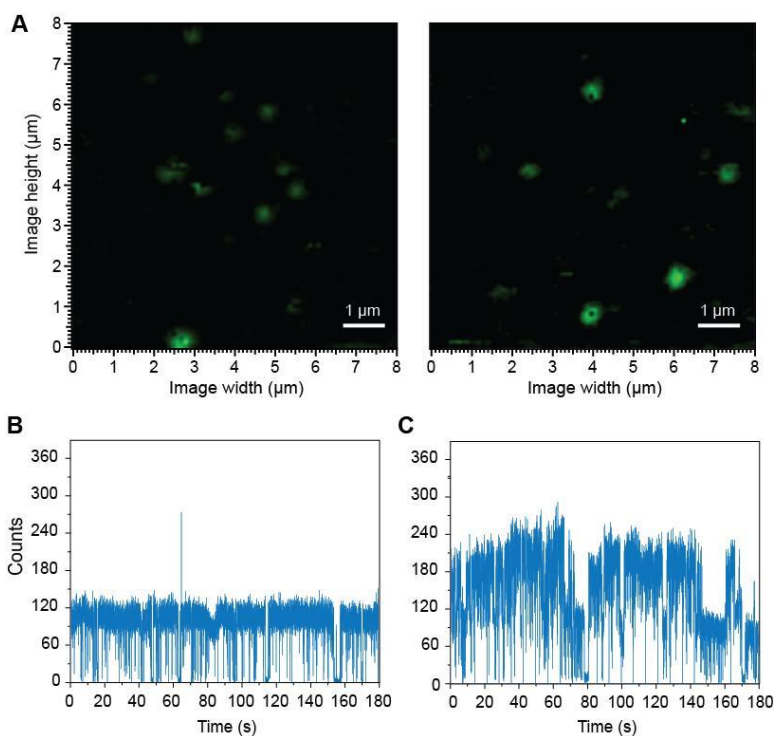


Figure 1. (A) Representative QD fluorescence microscopy images and (B-C) blinking trace of free QDs at 100 pM. (B) shows a representative blinking trace from an individual QD, and (C) shows a representative blinking trace that can be attributed to a small QD aggregate. Of 27 QDs, 25 monomers (93%) were detected based on the observation of diffraction-limited spot size, binary blinking dynamics, and consistent emissive/non-emissive intensities.

but when several QDs are observed, all the individual trajectories add up to yield a quasi-continuous fluorescence signal. By looking at the microscopic fluorescence and associated blinking trace, it is relatively easy to distinguish single QDs from multiple QDs, even without a reference sample.

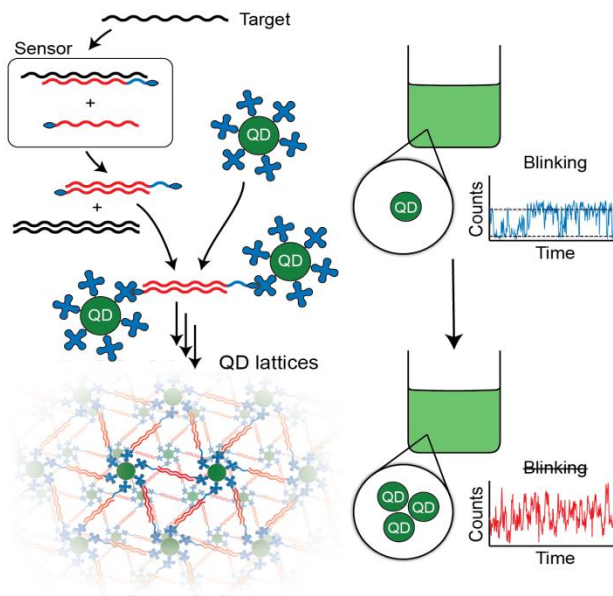


Figure 2. Schematics explaining the concept of biosensing with fluorescent blinking. Thermodynamically driven strand displacement in the presence of target sequence results in the formation of double biotinylated duplexes (in red) that upon addition of free quantum dots (QD) promotes formation of QD lattices. Additional blue section of the strand is required to stabilize biosensor formation.

To prove this concept, we designed a QD-based biosensor that uses a DNA strand-displacement method²¹⁻²⁶ to trigger the formation of QD lattices in the presence of a specific target strand as shown in Figure 2. Programmable DNA nano-assemblies²⁷⁻³⁰ have been shown to have an important impact in biosensing³¹⁻³⁵ and DNA is a well-suited biological material for the guided formation of QD assemblies because of its ability to self-assemble with its complementary strand.³⁶⁻³⁸ The working principle of our current biosensor is based on the thermodynamically driven re-association of DNA strands assisted

by ssDNA toeholds and triggered by a specific binding to target strand (a fragment of oncogene K-ras with codon 12 mutation).^{39,40} The re-association cascade leads to the formation of double biotinylated DNA duplexes, which rapidly cross-link the streptavidin-decorated QDs. Using confocal fluorescence microscopy we show that the target strand elicits a clear change in fluorescence trajectory from which we can infer the presence of the analyte and even estimate the number of particles in the resulting assemblies.

Experimental

Sequence design and sensor preparation

Single-stranded DNAs entering the composition of biosensors were designed by first designing the guard strand to complement the target mRNA strand. Then anti-guard strand was designed complementary to the guard strand with ssDNA toeholds. From there, we designed the DNA strand to complement the anti-guard strand. The guard and anti-guard strand were combined into a duplex that would detach in the presence of the target mRNA strand. Correct assemblies were tested with NUPACK.⁴¹ All oligos were purchased from Integrated DNA Technologies (IDT), Inc. All duplexes of the guard and anti-guard strand were assembled as detailed elsewhere.²⁶ All assemblies and re-association experiments were analyzed by non-denaturing polyacrylamide gel electrophoresis (native-PAGE). Formation of QD-based lattices was analyzed with agarose gels.

Confocal imaging

QD-biosensor solutions were analyzed by laser scanning confocal microscopy. Excitation was provided by a PicoQuant PDL 800-B pulsed laser with a LDH Series 470 nm laser head at a 10 MHz repetition frequency and power of 1.15 μW. Excitation pulses were coupled into a single-mode optical fiber, then directed to a 500 nm cutoff dichroic beam splitter before being focused onto the sample by a Zeiss 100x 1.25 NA oil immersion objective lens.

Results and Discussion

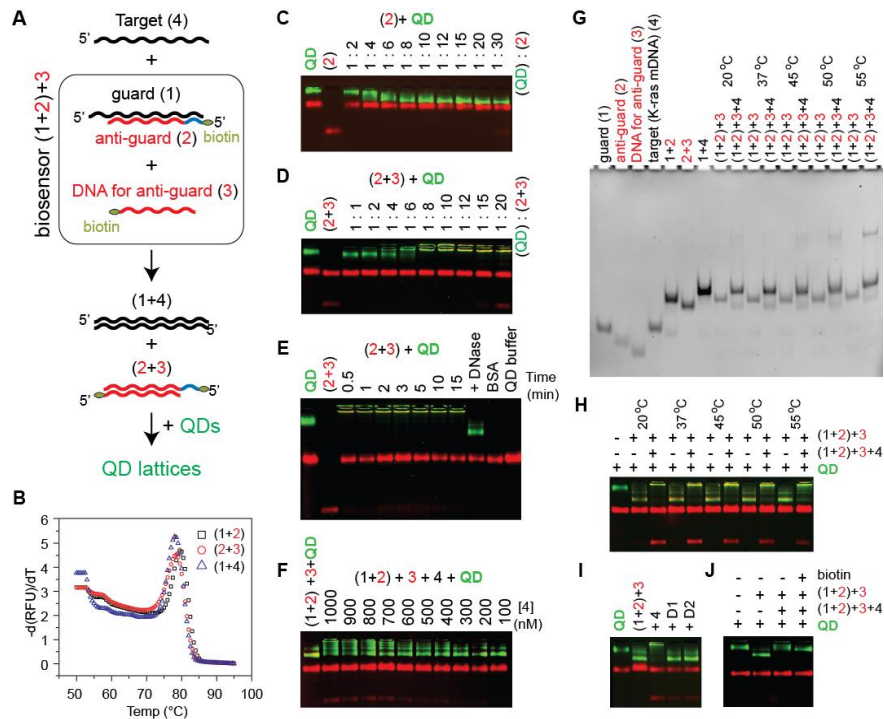


Figure 3. Recognition of target nucleic acids by programmable biosensor. (A) Schematics for biosensor. (B) Melting temperatures measured for all biosensing duplexes. (C) Titration experiments determined the highest number of biotinylated DNAs bound to QDs. (D) Titration experiments determined the ratio of double biotinylated (2+3) duplexes to QDs required for lattice formation. (E) Time course of QD lattices formation and treatment of QD lattices with DNase. Red bands appear due to composition of the QD buffer that contains BSA. (F) Detection limit of target strand driven formation or QD lattices with series of dilutions performed in QD buffer. (G) Total EtBr staining native-PAGE showing the strands displacement and biosensor activation (formation of 2+3) upon the presence of target strand (4). DNA for anti-guard strand (3) is the shortest and appears dim in (1+2)+3 lanes, however the formation of (2+3) duplexes is well observed in the following lanes. (H) Target strand triggered formation of QD lattices. For (G-H) different incubation temperatures were tested. (I) Target-specific formation of QD lattices is promoted by target (4) and not by “dummy” strands (D1 or D2). (J) The formation of QD lattices is abolished in the presence of biotin.

The proof-of-concept biosensor is schematically explained in Figure 3A. A target (4) interacts specifically with the guard DNA (1), releasing a biotinylated DNA strand (2), which can then re-associate with a complimentary strand (3) to form duplexes with two biotins (2+3). These can then crosslink streptavidin decorated QDs, yielding QD lattices. The lengths of the toeholds were defined based on the re-association rules described elsewhere⁴². The free energies of secondary structures were calculated⁴¹ to be -77 kcal/mol for (1+2) duplex, -65 kcal/mol for (2+3) duplex, and -97 kcal/mol for (1+4) duplex. The difference of -12 kcal/mol prevents (2+3) duplex formation in biosensor set up ((1+2)+3). However, the presence of target strand makes the formation of (2+3) more favorable, by -85 kcal/mol, due to (1+4) association. The melting temperatures shown in Figure 3B for all duplexes were measured to be 79.5 (77.8) °C for (1+2) duplex, 78.5 (76.3) °C for (2+3) duplex, and 78 (78) °C for (1+2) duplex and are in agreement with the predicted values (shown in parentheses).

Multiple electrophoretic mobility shift assays (Figure 3C-I) were done, prior to blinking analysis, to verify the working principle of this design. First, titration experiments showed that the maximum number of streptavidin-biotin interactions per QD was ~15-20 (Figure 3C). Due to the increase of overall negative charge of QDs upon DNA binding, their migration rate increases dramatically. However, the formation of lattices, makes it impossible for QDs to enter the agarose gel because of size limitations. We found (Figure 3D) that at least a 4:1 ratio of (2+3) duplexes to QDs were required for lattice formation. By mixing the pre-formed

(2+3) duplexes with QDs (Figure 3E), the complete conversion of free QDs into the lattices was found to take just 30 seconds and the lowest concentration of (2+3) duplexes required to visualize lattices with the gels was ~5 nM (Figure 3F). We showed that QD lattices can be easily digested by DNase, releasing free QDs with shorter DNA fragments attached (supporting Figure 3E). This experiment additionally confirms that the lattice formation is driven by DNAs.

To test the re-association of DNA strands in biosensor and the release of (2+3) duplexes, a series of assemblies with and without target strands present were analyzed by native-PAGE (Figure 3G). Re-association experiments were carried out at different incubation temperatures and the results confirm that the target sequence (4) causes the formation of (1+4) duplexes that result in the release of the biotinylated (2+3) duplexes. (2+3) duplexes were released most efficiently at an incubation temperature of 37°C. In the same set of experiments, QDs were added to the biosensor ((1+2)+3) with and without target strands (4) and analyzed on agarose gels, as shown in Figure 3H. Cleanest formation of QD lattices occurred at 20°C and 37°C. To test for specificity, two different “dummy” target strands of comparable lengths were tried (Figure 3I). Lattice formation was detected only in the presence of the correct target strands and was completely abolished in the presence of free biotin (Figure 3J).

Higher order bands were sometimes observed in re-association experiments with the target strand, especially when elevated incubation temperatures (45°C, 50°C, and 55°C) were used (Figure 2F). These bands were located higher than expected for double stranded DNA and point to energetically

stable complexes composed of more than two nucleic acids. These complexes decrease the efficiency of lattice formation (Figure 3G) by producing smear bands. To try and explain these bands we chose one possible complex composed of guard, anti-guard, and target (1+2+4), and ran MD simulations at four different temperatures: 27°C, 55°C, 60°C and 95°C. Simulation results indicate that target, guard, and anti-guard strands can form a stable complex which can be maintained at high temperature (55-60°C) and can therefore explain the additional bands observed when the target strand is present.

Representative fluorescence micrographs (Figure 4A-B) show 75 μm square fields containing streptavidin decorated QDs mixed with sensor strands before (4A) and after (4B) the target strand was introduced. The samples were analyzed at ~ 100 picomolar concentrations, which produced relatively dense particle distributions (Figs. 4A-B), which points towards the feasibility of using much lower QD concentrations. Both images are scaled to the same intensity ranges, and apart from a few brighter spots in Figure 4B, there is little visual difference between them. Small regions in Figs. 4A and B were reimaged and

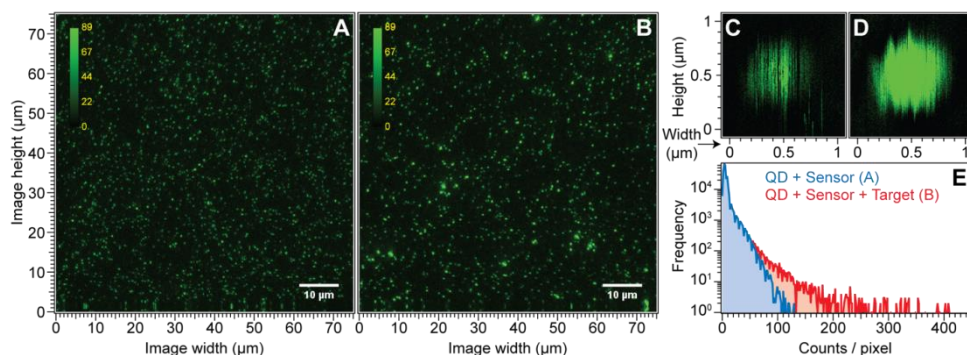


Figure 4. Representative QD fluorescence microscopy images. (A) QDs incubated with the biosensor (1:10 ratio). (B) QDs incubated with biosensor after addition of target strand. (C) Single QD re-imaged from the field in (A), exhibits streaking due to blinking. (D) QD aggregate from B, exhibits little streaking. (E) Intensity histograms for the images in A and B

are shown in Figs. 4C and D, respectively. Diffraction limits the resolution of the fluorescence spots to about 250 nm, so even moderately large QD lattices cannot be distinguished from single QDs by spot size alone; however, the particle in Figure 4C exhibits streaking in the fluorescence image, which is largely absent from the particle in Figure 4D. The streaking is due to blinking during a vertical raster scan across the particle and it indicates the presence of a single QD. The absence of streaking in Figure 4D strongly implies that multiple QDs are located within the focal spot. Note that in the absence of the target strand, the majority (>90%) of observed particles exhibited single QD blinking dynamics, while just a few were indicative of small groups of co-localized QDs (estimated 2-3 particles).

Further evidence of lattice formation comes from analysis of the intensity distribution in Figs. 4A and B, shown in Figure 4E. In the presence of the target strand the intensity histogram (red curve, corresponding to Figure 4B) has a significantly longer tail than the histogram recorded before target strand was added (blue curve, corresponding to Figure 4A). The presence of high intensity spots in Figure 4B indicates the presence of QD lattices that have many QDs within the detection volume, all of which can contribute to the fluorescence intensity.

The key results that distinguish QD lattices (formed after introduction of target strands) from individual QDs are presented in Figure 5. Representative fluorescence blinking traces recorded on a bright spot from Figs. 4A and B are shown in Figs. 5A and B, respectively. Each trace has been scaled over the

same intensity range. The blue trace in Figure 5A fluctuates randomly between bright (~380 counts/ 10 ms) and dark (~90 counts/10 ms) periods and is typical for a single QD. An intensity histogram calculated for this trace (Figure 5C), shows two peaks indicating the two intensity distributions.

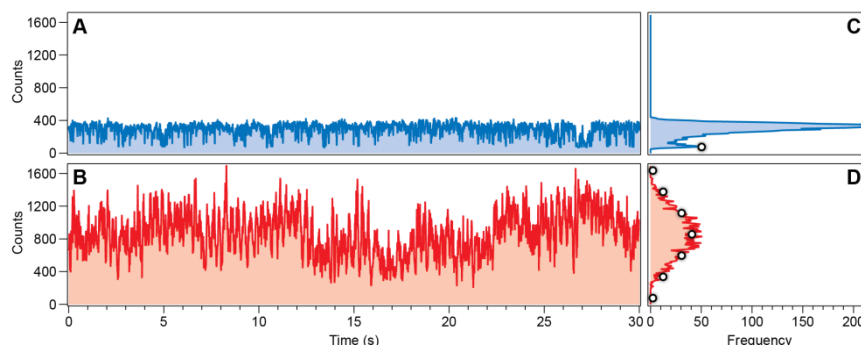


Figure 5. Representative blinking traces. **A:** Recorded on a bright spot in a fluorescence image from QDs incubated with biosensor (1:10 ratio). **B:** Recorded from a bright spot from QDs plus biosensor after incubation with target strands. Corresponding intensity histograms are shown in **C** and **D**. The white dots in **D** are derived from the two white intensity markers in **C** using a binomial model described in the text.

After introduction of the target strand the blinking trace in Figure 5B looks considerably different. Instead of binary blinking, the intensity fluctuates over a much wider range, indicating the lattice formation. Although particles in the lattices are still blinking, the total fluorescence for the whole lattice is rarely completely dark or fully bright. This is reflected in the blinking histogram (Figure 5D), which shows a broad intensity distribution with a mean intensity much greater than Figure 5C.

Assuming stochastic and independent blinking from each QD in a lattice we used a binomial model with single QD bright and dark intensities from Figure 5C (marked by open circles) to predict the expected blinking histograms for QD lattices. The intensity distribution for six QDs closely matches the measured

distribution in Figure 5D (open circles), suggesting that there are at least six emitting QDs in this particular lattice.

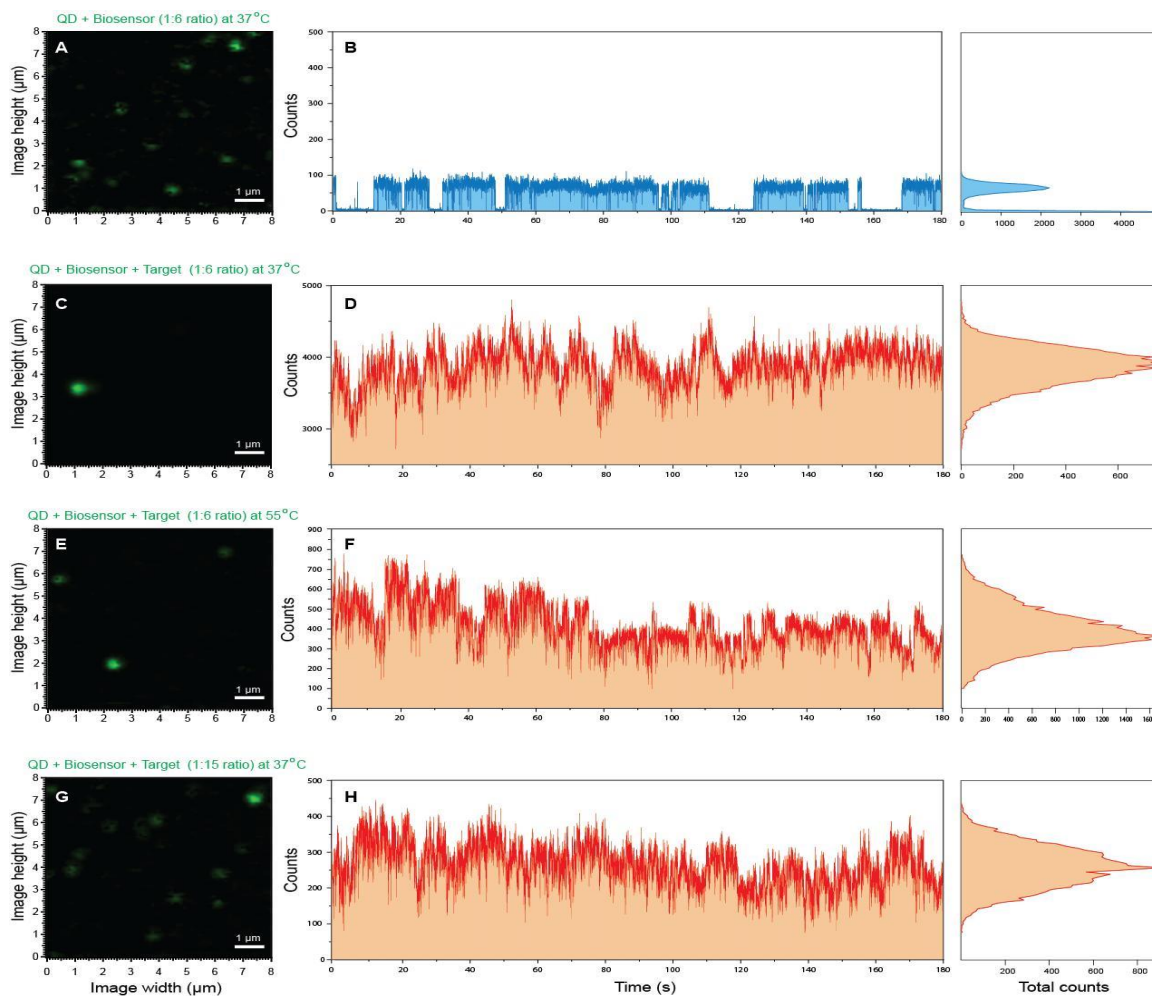


Figure S6. Fluorescence microscopy images and corresponding blinking traces of **A-B**: QDs + sensor (at 1:6 ratio), **C-D**: QDs + sensor (1:6) after incubation with target strands at 37°C, **E-F**: QDs + sensor (1:6) after incubation with target strands at 55°C measured, and **G-H**: QDs + sensor (1:15) after incubation with target strands at 37°C. All samples were analyzed at 800 pM concentration.

This type of analysis is approximate since it relies on the intensity of an unrelated single QD as a basis for the intensity distribution of the QD lattice; however, we illustrate in Figure 6 the intensity distributions expected from lattices containing different numbers of QDs. When the biosensor is not in the presence of the target strand, the QDs do not form a lattice and exhibit binary blinking

(Figure 6A-B). Once the target strand is added, we observe that the biosensors detect the target strand, which ensures formation of the QD lattice (Figure 6C-H). The QD lattices emit quasi-continuous blinking with relatively great intensity, even at varying incubation temperatures and ratios with the sensor, which attests to the versatility of the QD and biosensor design.

The difference in blinking dynamics provides us with a reference-free way to distinguish the presence of QD lattices triggered by the addition of a target strand. A sample that yields bright spots with bimodal trajectories, like Figure 5A, clearly contains single QDs, while a sample that yields widely distributed intensity trajectories, like Figure 5B, must contain aggregated QD lattices and therefore indicates the presence of the target strand. The concentration of QD lattices required for the blinking study is in the picomolar range, which would be hard to detect using ensemble fluorescence techniques. Although the analytical performance of this method is a complex function of the absolute concentrations of sensor and target strands as well as QD concentration, false positives can be eliminated by surveying a representative number of fluorescent spots. Finally, we recognize that single particle fluorescence microscopy is complex compared to the ensemble techniques used in other QD biosensing methods; however, previous studies have demonstrated the integration of confocal fluorescence with microfluidics for single particle analysis, which suggests that our proposal is realistic.^{43,44}

Conclusion

In conclusion, we have demonstrated, for the first time, the application QD fluorescence blinking for biosensing. As a proof of concept, we constructed a DNA-based sensor that triggered QD lattice formation after introduction of a target molecule. These lattices could then be unequivocally identified by analysis of blinking trajectories using picomolar QD concentrations. Although this is currently a binary sensor, further investigation of the blinking response in different sized lattices or with different inter-particle distances could enable us to distinguish a wider range of situations. We anticipate that the current technique can also find multiple applications in the emerging field of RNA nanotechnology⁴⁵⁻⁴⁸ as a quick and parsimonious method for visualization of various programmable assemblies and their interactions.

Acknowledgments

This was a collaborative study led by Brandon Roark, Marcus Jones, Kirill A. Afonin from the University of North Carolina at Charlotte. We acknowledge fellow collaborators: Anna Ivanina, Morgan Candler, Jose Castaneda, Ho Shin Kim, Shriram Jawahar, Mathias Viard, Strahinja Talic, and Yaroslava G. Yingling (North Carolina State University, National Cancer Institute, Frederick National Laboratory for Cancer Research). We thank Dr. Troutman (UNC Charlotte) for helpful discussion. This publication was funded with the start-up funds provided by UNC Charlotte to KAA. HSK and YGY acknowledge support by NSF (CMMI-1150682). The computer support was provided by High Performance Computing

(HPC) center at North Carolina State University. This work has been funded in whole or in part with Federal funds from the Frederick National Laboratory for Cancer Research, National Institutes of Health, under Contract No. HHSN261200800001E.

References

- (1) Ho, Y. P.; Leong, K. W. Quantum dot-based theranostics. *Nanoscale* **2010**, *2*, 60-68.
- (2) Chou, K. F.; Dennis, A. M. Forster Resonance Energy Transfer between Quantum Dot Donors and Quantum Dot Acceptors. *Sensors (Basel)* **2015**, *15*, 13288-13325.
- (3) Kovtun, K.; Arzeta-Ferrer, X.; Rosenthal, S.J. Quantum Dot Approaches for Target-Based Drug Screening and Multiplexed Active Biosensing. *Nanoscale* **2013**, *5*, 12072-12081.
- (4) Liu, C.; Kim, K.; Fan, D. L. Location deterministic biosensing from quantum-dot-nanowire assemblies. *Appl Phys Lett* **2014**, *105*, 083123.
- (5) Mattoussi, H.; Medintz I.L., Clapp A.R., Goldman E.R., Jaiswal, J.K., Simon, S.M., Mauro, J.M. Luminescent Quantum Dot-Bioconjugates in Immunoassays, FRET, Biosensing, and Imaging Applications. *JALA* **2004**, *9*, 28-32.
- (6) Zhou H., L. J., Zhang S. Quantum-Dot Based Photoelectric Conversion for Biosensing. *TrAC* **2015**, *67*, 56-73.
- (7) Wang, Y.; Hu, R.; Lin, G.; Roy, I.; Yong, K. T. Functionalized quantum dots for biosensing and bioimaging and concerns on toxicity. *ACS applied materials & interfaces* **2013**, *5*, 2786-2799.
- (8) Resch-Genger, U.; Grabolle, M.; Cavaliere-Jaricot, S.; Nitschke, R.; Nann, T. Quantum dots versus organic dyes as fluorescent labels. *Nature methods* **2008**, *5*, 763-775.
- (9) Wegner, K. D.; Hildebrandt, N. Quantum dots: bright and versatile in vitro and in vivo fluorescence imaging biosensors. *Chemical Society reviews* **2015**, *44*, 4792-4834.
- (10) Chakravarthy, K. V.; Davidson, B. A.; Helinski, J. D.; Ding, H.; Law, W. C.; Yong, K. T.; Prasad, P. N.; Knight, P. R. Doxorubicin-conjugated quantum dots to target alveolar macrophages and inflammation. *Nanomedicine* **2011**, *7*, 88-96.
- (11) Lee, T.; Yagati, A. K.; Pi, F.; Sharma, A.; Choi, J. W.; Guo, P. Construction of RNA-Quantum Dot Chimera for Nanoscale Resistive Biomemory Application. *ACS nano* **2015**, *9*, 6675-6682.
- (12) Zhou, J.; Yang, Y.; Zhang, C. Y. Toward Biocompatible Semiconductor Quantum Dots: From Biosynthesis and Bioconjugation to Biomedical Application. *Chemical reviews* **2015**, *115*, 11669-11717.
- (13) Oh, J. H.; Park do, H.; Joo, J. H.; Lee, J. S. Recent advances in chemical functionalization of nanoparticles with biomolecules for analytical applications. *Analytical and bioanalytical chemistry* **2015**, *407*, 8627-8645.
- (14) Freeman, R.; Girsh, J.; Willner, I. Nucleic acid/quantum dots (QDs) hybrid systems for optical and photoelectrochemical sensing. *ACS applied materials & interfaces* **2013**, *5*, 2815-2834.
- (15) Li, J.; Zhu, J. J. Quantum dots for fluorescent biosensing and bio-imaging applications. *The Analyst* **2013**, *138*, 2506-2515.
- (16) Chan, P.; Yuen, T.; Ruf, F.; Gonzalez-Maeso, J.; Sealfon, S. C. Method for multiplex cellular detection of mRNAs using quantum dot fluorescent in situ hybridization. *Nucleic acids research* **2005**, *33*, e161.
- (17) Zhang, W.; Hubbard, A.; Brunhoeber, P.; Wang, Y.; Tang, L. Automated multiplexing quantum dots in situ hybridization assay for simultaneous detection of ERG and PTEN gene status in prostate cancer. *The Journal of molecular diagnostics : JMD* **2013**, *15*, 754-764.
- (18) Feng, C. L.; Zhong, X. H.; Steinhart, M.; Caminade, A. M.; Majoral, J. P.; Knoll, W. Graded-Bandgap Quantum- Dot-Modified Nanotubes: A Sensitive Biosensor for Enhanced Detection of DNA Hybridization. *Adv Mater* **2007**, *19*, 1933-1936.
- (19) Hansen, J. A.; Wang, J.; Kawde, A. N.; Xiang, Y.; Gothelf, K. V.; Collins, G. Quantum-dot/aptamer-based ultrasensitive multi-analyte electrochemical biosensor. *Journal of the American Chemical Society* **2006**, *128*, 2228-2229.
- (20) Efros, A. L.; Rosen, M. Random Telegraph Signal in the Photoluminescence Intensity of a Single Quantum Dot. *Physical review letters* **1997**, *78*, 1110-1113.
- (21) Seelig, G.; Soloveichik, D.; Zhang, D. Y.; Winfree, E. Enzyme-free nucleic acid logic circuits. *Science* **2006**, *314*, 1585-1588.
- (22) Turberfield, A. J.; Mitchell, J. C.; Yurke, B.; Mills, A. P., Jr.; Blakey, M. I.; Simmel, F. C. DNA fuel for free-running nanomachines. *Physical review letters* **2003**, *90*, 118102.

- (23) Machinek, R. R.; Ouldrige, T. E.; Haley, N. E.; Bath, J.; Turberfield, A. J. Programmable energy landscapes for kinetic control of DNA strand displacement. *Nature communications* **2014**, *5*, 5324.
- (24) Srinivas, N.; Ouldrige, T. E.; Sulc, P.; Schaeffer, J. M.; Yurke, B.; Louis, A. A.; Doye, J. P.; Winfree, E. On the biophysics and kinetics of toehold-mediated DNA strand displacement. *Nucleic acids research* **2013**, *41*, 10641-10658.
- (25) Sulc, P.; Ouldrige, T. E.; Romano, F.; Doye, J. P.; Louis, A. A. Modelling toehold-mediated RNA strand displacement. *Biophysical journal* **2015**, *108*, 1238-1247.
- (26) Afonin, K. A.; Viard, M.; Martins, A. N.; Lockett, S. J.; Maciag, A. E.; Freed, E. O.; Heldman, E.; Jaeger, L.; Blumenthal, R.; Shapiro, B. A. Activation of different split functionalities on re-association of RNA-DNA hybrids. *Nature nanotechnology* **2013**, *8*, 296-304.
- (27) Pinheiro, A. V.; Han, D.; Shih, W. M.; Yan, H. Challenges and opportunities for structural DNA nanotechnology. *Nature nanotechnology* **2011**, *6*, 763-772.
- (28) Genot, A. J.; Bath, J.; Turberfield, A. J. Reversible logic circuits made of DNA. *Journal of the American Chemical Society* **2011**, *133*, 20080-20083.
- (29) Turberfield, A. J. DNA nanotechnology: geometrical self-assembly. *Nature chemistry* **2011**, *3*, 580-581.
- (30) Liedl, T. Nanotechnology: Pathfinder for DNA constructs. *Nature* **2015**, *523*, 412-413.
- (31) Liang, H.; Zhang, X. B.; Lv, Y.; Gong, L.; Wang, R.; Zhu, X.; Yang, R.; Tan, W. Functional DNA-containing nanomaterials: cellular applications in biosensing, imaging, and targeted therapy. *Accounts of chemical research* **2014**, *47*, 1891-1901.
- (32) Zhao, Y.; Chen, F.; Li, Q.; Wang, L.; Fan, C. Isothermal Amplification of Nucleic Acids. *Chemical reviews* **2015**.
- (33) Dirks, R. M.; Pierce, N. A. Triggered amplification by hybridization chain reaction. *Proceedings of the National Academy of Sciences of the United States of America* **2004**, *101*, 15275-15278.
- (34) Huang, D.; Niu, C.; Ruan, M.; Wang, X.; Zeng, G.; Deng, C. Highly sensitive strategy for Hg²⁺ detection in environmental water samples using long lifetime fluorescence quantum dots and gold nanoparticles. *Environmental science & technology* **2013**, *47*, 4392-4398.
- (35) Huang, D.; Niu, C.; Wang, X.; Lv, X.; Zeng, G. "Turn-on" fluorescent sensor for Hg²⁺ based on single-stranded DNA functionalized Mn:CdS/ZnS quantum dots and gold nanoparticles by time-gated mode. *Analytical chemistry* **2013**, *85*, 1164-1170.
- (36) Mirkin, C. A.; Letsinger, R. L.; Mucic, R. C.; Storhoff, J. J. A DNA-based method for rationally assembling nanoparticles into macroscopic materials. *Nature* **1996**, *382*, 607-609.
- (37) Mitchell, G. P., Mirkin C.A., R.L. Letsinger. Programmed Assembly of DNA Functionalized Quantum Dots. *JACS* **1999**, *121*, 8122-8123.
- (38) Sharma, J.; Ke, Y.; Lin, C.; Chhabra, R.; Wang, Q.; Nangreave, J.; Liu, Y.; Yan, H. DNA-tile-directed self-assembly of quantum dots into two-dimensional nanopatterns. *Angew Chem Int Ed Engl* **2008**, *47*, 5157-5159.
- (39) Kam, Y.; Rubinstein, A.; Nissan, A.; Halle, D.; Yavin, E. Detection of endogenous K-ras mRNA in living cells at a single base resolution by a PNA molecular beacon. *Mol Pharm* **2012**, *9*, 685-693.
- (40) Minamoto, T.; Mai, M.; Ronai, Z. K-ras mutation: early detection in molecular diagnosis and risk assessment of colorectal, pancreas, and lung cancers--a review. *Cancer detection and prevention* **2000**, *24*, 1-12.
- (41) Zadeh, J. N.; Steenberg, C. D.; Bois, J. S.; Wolfe, B. R.; Pierce, M. B.; Khan, A. R.; Dirks, R. M.; Pierce, N. A. NUPACK: Analysis and design of nucleic acid systems. *J Comput Chem* **2010**, *32*, 170-173.
- (42) Bindewald, E.; Afonin, K. A.; Viard, M.; Zakrevsky, P.; Kim, T.; Shapiro, B. A. Multistrand Structure Prediction of Nucleic Acid Assemblies and Design of RNA Switches. *Nano letters* **2016**, *16*, 1726-1735.
- (43) Heus, F.; Giera, M.; de Kloe, G. E.; van Iperen, D.; Buijs, J.; Nahar, T. T.; Smit, A. B.; Lingeman, H.; de Esch, I. J.; Niessen, W. M.; Irth, H.; Kool, J. Development of a microfluidic confocal fluorescence detection system for the hyphenation of nano-LC to on-line biochemical assays. *Analytical and bioanalytical chemistry* **2010**, *398*, 3023-3032.

- (44) Puleo, C. M.; Yeh, H. C.; Liu, K. J.; Wang, T. H. Coupling confocal fluorescence detection and recirculating microfluidic control for single particle analysis in discrete nanoliter volumes. *Lab on a chip* **2008**, *8*, 822-825.
- (45) Afonin, K. A.; Kasprzak, W. K.; Bindewald, E.; Kireeva, M.; Viard, M.; Kashlev, M.; Shapiro, B. A. In silico design and enzymatic synthesis of functional RNA nanoparticles. *Accounts of chemical research* **2014**, *47*, 1731-1741.
- (46) Afonin, K. A.; Desai, R.; Viard, M.; Kireeva, M. L.; Bindewald, E.; Case, C. L.; Maciag, A. E.; Kasprzak, W. K.; Kim, T.; Sappe, A.; Stepler, M.; Kewalramani, V. N.; Kashlev, M.; Blumenthal, R.; Shapiro, B. A. Co-transcriptional production of RNA-DNA hybrids for simultaneous release of multiple split functionalities. *Nucleic acids research* **2014**, *42*, 2085-2097.
- (47) Guo, P. The emerging field of RNA nanotechnology. *Nature nanotechnology* **2010**, *5*, 833-842.
- (48) Khisamutdinov, E. F.; Jasinski, D. L.; Guo, P. RNA as a boiling-resistant anionic polymer material to build robust structures with defined shape and stoichiometry. *ACS nano* **2014**, *8*, 4771-4781.

APPENDIX II: TIME-CORRELATED SINGLE PHOTON COUNTING STUDIES FOR SENSITIZERS

Background

Dye-sensitized solar cells (DSSCs) are an inexpensive alternative to conventional silicon-based solar cells, but their efficiencies have plateaued at ~13%.¹⁻³ The performance of DSSCs is related to the interfacial electron transfer (ET) kinetics between the dye sensitizer and semiconductor. Extensive studies of the ET kinetics at the excited state demonstrate that electron injection of dye-TiO₂ systems occur at subpicosecond timescales, which are 2-5 orders of magnitude faster than radiative decay from the excited state to the ground state.⁴⁻⁵ Thus, electron injection is generally not considered a limiting factor for device efficiency. Yet, studies find that interfacial ET kinetics are complex and multiphasic,⁶⁻¹² with recent studies reporting that electron injection can actually occur on a range of timescales from subpicoseconds down to seconds.⁶⁻¹⁰ This vast range of timescales can be problematic for efficient electron injection due to competition between the different kinetic processes following photoexcitation. According to equation 11, the lifetime of the excited state (τ_{on}) is dependent upon the rate constant for excitation (k_{12}), dark-state population (k_{23}), and emission (k_{21}):

$$\tau_{on} = \left[\left(\frac{k_{23}}{k_{23} + k_{21}} \right) k_{12} \right]^{-1} \quad (1).^{11,15}$$

In a dye-TiO₂ system, k_{23} and k_{21} represent the rate constants for electron injection and fluorescence, respectively. In an ideal system, electron injection should occur only on the ultrafast timescales (e.g., femtoseconds - picoseconds),

while fluorescence operates on the nanosecond timescale. If electron injection occurs much more slowly, it can operate in the same time regime as fluorescence, which introduces kinetic competition between the two processes at the excited state. This competition can decrease the efficiency of electron injection into the conduction band of the semiconductor, which reduces the productivity of a DSSC. Therefore, investigating the excited state in a dye-TiO₂ system will provide further insight into the dispersive ET kinetics.

Obtaining measurements on fluorescence lifetimes can yield insight into the complexities of the interactions of the kinetic processes in a dye-TiO₂ system. The fluorescence lifetime (τ_{fl}) is a convolution of fluorescence (k_{fl}) and injection (k_{inj}) dynamics along with non-radiative processes (k_{nr}) according to:

$$\tau_{fl} = \left[\frac{k_{fl}}{k_{fl} + k_{inj} + k_{nr}} \right]^{-1} \quad (2).^{11,15}$$

In particular, time-correlated single photon counting (TCSPC) is a well-established technique to exploring molecular photophysics by measuring and analyzing fluorescence decay curves.¹³⁻¹⁷ Several properties of a fluorophore can be probed by TCSPC including fluorescence quantum yield, fluorescence lifetime, and anisotropy.¹⁷ TCSPC is based upon the detection of single photons – the arrival time of these fluorescent photons with respect to an exciting laser pulse is recorded by spectrally resolved and polarized detection channels.¹⁵⁻¹⁷ By generating histograms of the relative times of photon arrival, the fluorescence kinetics decay curve is constructed.¹³⁻¹⁷ TCSPC is an ideal technique for capturing multicomponent decays and ultrafast processes (i.e., femtosecond timescale) because of its high sensitivity, fast response, and dynamic range.¹⁴⁻¹⁷

Moreover, when light levels are low, such as in single-molecule experiments, TCSPC is a valuable method to those studies since it can detect very low photon counts.¹⁴ We seek to increase our understanding of ET dynamics with by probing the excited state of single fluorophores in a DSSC system.^{12,22} This section is intended to serve as a guide for conducting TCSPC studies on various samples and fitting fluorescence decays. The appendix is not a formal TCSPC discussion but outlines and provides explanations for the major steps to be carried out in our lab setup. This appendix should also be read with the TCSPC standard operating procedures located in the shared lab binder.

Experimental

Confocal Microscopy and Instrument Response Function

The following experimental setup in this section is done regardless of the sample choices (i.e., thin film or single molecule). Microscope setup for TCSPC studies is nearly identical to SMS studies. Essentially, I follow the same procedures for setup and bead alignment, which involve: placing beads for 470 nm excitation in the flow cell atop the objective and piezoelectric stage; aligning the laser through the optics and periscope; and obtaining raster-scanned images of the beads after aligning the detector. The first major difference between TCSPC and SMS setup is that I use the pulsed mode of the 470 nm laser instead of continuous wave (CW) excitation. Using the pulsed mode of the 470 nm laser leads to a decrease in the average power relative to the CW mode (as measured by our power meter). However, each pulse has its own power, which is much

larger than the average power. For any TCSPC study, the intensity setting must be set above the lasing threshold, which was measured to be at 6.0. The frequency setting of the pulsed mode is more versatile because that is dependent on your sample. Fast frequencies (i.e., 80 MHz) will give more power with each pulse, while slower frequencies (i.e., 1 kHz) will give less power with each pulse and lead to an overall decrease in average power. To obtain images of beads, I normally used a frequency of 20 MHz and an intensity setting of 6.0 because I could adjust the power being sent to the beads with the waveplate and the use of the ND4 filter. The second difference between TCSPC and SMS studies is that the 470 nm dichroic beamsplitter is required and not optional like in SMS studies. The dichroic beamsplitter ensures careful wavelength selection of the photons that will excite the sample and pass through to the detector from sample emission. The emission filter will still be used since it acts as a general blocker of photons from the laser excitation of choice.

Now I obtain the control measurement necessary for TCSPC studies, which is the instrument response function (IRF). For SMS studies, the control is obtaining well-defined images of beads in order to establish an aligned laser and detector. TCSPC studies still require beads in order to align the laser and detector, but we need to determine the background contribution to a sample's fluorescence decay signal. The background contribution is represented by the IRF, which can then be accounted when fitting a sample's fluorescence decay. The IRF is essentially a fluorescence decay measurement of a non-fluorescing sample to measure only the scattered emission from the laser. The width of the

IRF reports on how well the laser is aligned and the impact of the overall instrument setup on the laser excitation. Generally, the laser has an exceedingly small pulse width, (i.e., our laser tech manual indicates it should have a pulse width of ~68 ps),¹⁹ so the fluorescence decay should look like a very narrow Gaussian distribution that is only picoseconds or smaller in width. An IRF that is exactly the same width as the laser pulse width would only be expected with very refined and sensitive instruments coupled with perfect alignment. In other terms, the IRF provides us with a measurement of how much noise is being contributed by our instrument setup to the laser excitation.^{15,16,19,20} The purpose of the IRF in fitting analysis will be discussed in the analysis section.

Obtaining an IRF measurement is straightforward. The necessary “sample” is something that will scatter light and not fluoresce, which can be done with bare glass or a colloidal solution, such as milk. I turn off the piezoelectric stage and SPAS program, since they are not needed for lifetime measurements. However, I keep the piezoelectric stage atop the confocal microscope because it provides the height necessary to lay samples atop the objective. I use a bare basebathed coverslip (or rinse a coverslip with ethanol) and carefully lay the coverslip on top of two microscope slides, which act as ledges on top of the piezoelectric stage. I recommend placing a black cloth over the detector (but not blocking the pathway from the microscope to the detector) in order to ensure that minimal light is detected, since the TCSPC module coupled with the detector is sensitive to light. The frequency and intensity settings should be set to the experimental settings, so that the IRF and fluorescence samples’ fluorescence

decays are measured at the same settings. However, the waveplate and choice of ND filter will be variable.

At this point, I turn on the TCSPC module and the PicoHarp program, which is where I can control the fluorescence decay collections. There are channels at the bottom of the program which display the frequency of the laser in one channel, and the number of counts being detected in another channel. The number of counts being detected by the detector should be smaller than 1 percent of the laser's frequency.^{20,21} For example, if I use a 10 MHz repetition rate (i.e., 10×10^7 counts), the number of counts being detected by the detector should be 10,000. This is necessary to ensure that only one photon will be detected in between pulses. If there are too many counts relative to the frequency of the laser, that increases the possibility of two photons or more occurring in between a pulse, but only one will be tagged by the TCSPC module.^{20,21} My general rule of thumb is that I try to decrease the number of counts detected to even lower than 1%, as long as that does not make the buildup of the fluorescence decay exceedingly slow (i.e., the peak of the decay does not exceed 10^3 counts after a 180 seconds acquisition). In reality, maintaining counts below 1% of the repetition rate will help ensure the maintenance of the detector.

Other settings that should be adjusted include acquisition time and the offset of the decay. Acquisition length, unlike for a blinking trace, does not have to be identical between samples. I set the acquisition length so that I can collect approximately 10^4 counts if possible within 3-4 minutes. Any longer than that,

and I would need to worry about sample degradation. Also, I have noticed that increasing acquisition times does not necessarily increase the signal of the decay. I sometimes will simply observe an increase of both the baseline and the decay, which is meaningless. As long as the number of counts collected for the decay is around 10^3 or more, that should be sufficient for fitting analysis. Furthermore, the start of the decay should not start at exactly 0 ps because our fitting program requires some baseline noise before the start of the decay in order to fit properly.^{20,22} Therefore, I shift the beginning of the decay slightly (i.e., 35000 ps). The module and program recognize that the shift is for artificial purposes, and the photon arrival time is absolute. Since I use bare glass for IRF measurements, I collect photons for no longer than 120 seconds to build up my fluorescence decay curve. It is useful at the end of each decay collection to not only save the file as a .phu format but also as an ASCII file for future figure workups.

Lifetime Standards or Solution Measurements

This section will review how to measure the lifetimes of solutions that are not spuncoat. A lifetime standard measurement relies on fluorophores that have single exponential decay lifetimes consistently measured by different studies. Unfortunately, most studies use a fluorimeter capable of the TCSPC technique, so a cuvette of the fluorophore is measured. We have to improvise since we are a bit unusual and use a confocal microscope setup for TCSPC measurements. Boens et al. compared single-exponential lifetimes of common fluorophores

between different labs and is a reliable source to compare your standard lifetime measurements.²³ I use an ethanol-cleaned coverslip only because a base-bathed coverslip does not allow for liquid surface tension. I place the coverslip atop the microscope slide ledges and slowly drop my prepared liquid sample 20 uL at a time. A large droplet should form on the slide (whereas on a basebathed slide, the solution will simply sprawl everywhere). A conservative amount would be 100 uL. As long as there is still a glass rim around the droplet, I use variable amounts of the solution.

I then carry out the steps outlined for IRF collection, where I will use the same frequency and intensity settings. However, I adjust the waveplate and ND filter in order to ensure that less than 1% ratio between the laser's frequency and the number of counts being detected. I suggest that power is measured after the setting is determined, rather than trying to predict the power to use based on the power chart. Be careful about not spilling the sample on the microscope! I have a petri dish beside me, so I can quickly dump the sample and slide into the dish. Fluorescein is an excellent lifetime standard for TCSPC beginners to practice obtaining lifetime measurements and practice fitting procedures.

Thin-Film Samples

The aggregate manuscript has a formal explanation of how the samples were made and measured.²⁴ Here I will simplify how to collect lifetime measurements on thin-film samples. Thin-film samples should be prepared on coverslips, not microscope slides, in order for the focus of the laser to reach the

sample. The thin-film samples are placed atop the microscope slide ledges, similar to the IRF and solution measurements. I will keep the frequency and intensity settings constant for all measurements for the experiment, but once again, I must adjust the waveplate and ND filter choice. With heavily dyed samples, that adjustment can occur frequently between decay collections. Since thin films have a heterogeneous surface, I obtain multiple decay curves corresponding to each thin-film sample. For example, when I looked at a dye-loading concentration of 10^{-5} M R560 on a TiO_2 thin film, I collected fluorescence decays on 10 different spatial locations on the films. I simply shifted the thin film in a raster pattern with my tweezers to ensure I did not excite the same spot.

General Recommendations and Troubleshooting

Focusing the laser for TCSPC studies is necessary but can be tricky. On bare glass, I use Ueye or look through the oculars to focus the laser. With liquid samples, I look at the number of counts being detected. A focused laser will have more counts than an unfocused laser, so I adjust the fine focus until I get roughly the maximum number of counts. Unfortunately, it is hard to get an exact focus with liquid measurements because the laser cannot be observed through the microscope. For thin-film samples, focusing the laser is dependent on the concentration. With low dye-loading concentrations, I can focus by eye once again. That is more difficult to accomplish with heavily-dyed samples, but you can still focus through the oculars by ensuring that the sample's surface is focused and not blurry. Furthermore, a focused laser will have a very bright spot.

If it is difficult to discern the focus or if I am uncertain, I will double check by watching the changes in counts detected as I adjust the fine focus.

The smallest IRF full-width at half-maximum (FWHM) I have obtained was ~128 ps. On average, I usually get from 130-140 ps. If I get a FWHM larger than that, I would revisit my laser and detector alignment. Usually, poor alignment or old beads contributed to a larger IRF. The IRF only needs to be measured at the beginning of the experiment, similar to taking a final bead scan once before SMS scans and blinking traces.

Low sample signal can make fitting difficult. As mentioned in previous sections, I like to have fluorescence decay curves where the peak has at least 10^3 counts or more. Normally, adjusting the waveplate setting and ND filter choice can give you enough power to excite the sample but have the number of counts detected be less than 1% of the laser's frequency. If adjusting the waveplate setting and ND filter does not work, then I would adjust the intensity setting of the laser and finally adjust the repetition frequency. That should be the last resort because changing the frequency can drastically change the power with each pulse being sent to the sample. Increasing acquisition time can help a little bit, but again, if the signal-to-noise ratio does not change significantly, then longer acquisition times will not help. If all of those changes do not help, then the sample's fluorescence is either weak or too sensitive for our TCSPC setup.

Fitting Emission Decay Analysis

Background and Statistical Fitting Parameters

The mantra for fitting fluorescence decay curves is to be conservative with fitting and interpretation.^{15,16,22} Unfortunately, the fitting software is more subjective than I would prefer, so intensive practice is necessary in order to gain perspective on the constitution of a good fit. Detailed instructions on using the software for fitting are kept with the operating procedures and manual for the software.²² In this appendix, I will elaborate on the rationale behind my choices and considerations for fitting.

Fitting fluorescence decay curves requires some knowledge of the system gained through other experimental methods or precedents in literature. Lifetime fits will rarely be used to describe the system because of the enormous variability involved in the fitting process. Another consideration is that even though observing fluorescence allows us to observe events on the nanosecond timescale, there are much faster photophysical events that we are missing (i.e., absorption). Why should we use TCSPC then? A major factor is that TCSPC and fluorescence experiments are much easier to conduct because we do not have to maintain an expensive and sensitive ultrafast laser (although fluorescence experiments can be carried out on a faster timescale with expensive instruments). Furthermore, we still gain valuable insight into the photophysics of a system to understand what happens after a molecule reaches the excited state.

Thus, if there is prior knowledge of the mathematical function that describes the system, I would start fitting my curve with the least number of fitting

parameters for that function.^{15,16} However, if there is not much prior knowledge, the exponential function is the simplest choice to begin fitting with the stretched exponential as the close second choice.^{15,16} There are other functions to choose from, but I would read about the types of systems that the alternative functions describe to determine if the alternatives to the exponential function are suitable.

When fitting decay curves, I always start out with the least number of fitting parameters, such as for an analysis with a single-exponential function.^{15,16,22} The exponential function takes the following form:

$$I(t) = \sum_{i=1}^n \alpha_i \exp\left(-\frac{t}{\tau_i}\right),$$

where α_i is the pre-exponential factor for the amplitudes of the exponential, and τ_i is the lifetime of the exponential decay.^{15,16,22} Fluorescence dynamics are fitted using the nonlinear least-squares reconvolution of the instrument response function (IRF, full width at half maximum (FWHM) ~130 ps) to discount the IRF contribution to the fluorescence decay.²² Good-fit criteria are described by a $\chi^2 \sim 1$, and a random distribution of weighted residuals around zero (looks flat).^{15,16,22} If χ^2 is larger than 2 and is coupled with weighted residuals that are not randomly distributed and have large deviations, I increase the number of fitting parameters (i.e., go from single exponential to bi-exponential).^{15,16,22}

However, meeting the good-fit criteria is not as straightforward as always increasing the number of fitting parameters. I can force my way to getting a $\chi^2 \sim 1$ and randomly distributed weighted residuals if I give the program a large number of fitting parameters to work with, which makes fitting more flexible for the program. A large number of fitting parameters does not necessarily yield any

physical significance in the fluorescence dynamics. This is where great caution must be exercised – to determine whether you an increase in the number of fitting parameters is necessary.

Quick Exercise

I have noticed that I can identify whether an increase in fitting parameter is unnecessary when one of the time components has a lifetime smaller than the IRF FWHM. For example, I obtain an IRF of 150 ps in my control study. When analyzing the decay with a single exponential fit, I obtain an amplitude of 10000 counts and a time component of 1.2 ns. The χ^2 is 1.3, and I have a small wave at the beginning of my IRF, but I wonder if I could get a better fit with a bi-exponential function. When I carry out that analysis, I obtain a $\alpha_1 = 7500$ and $\tau_1 = 1.1$ ns, and $\alpha_2 = 2500$ and $\tau_2 = 0.05$ ns (i.e., 50 ps). The χ^2 is 1.1 and my weighted residuals look relatively flat and randomly distributed.

Take notice that although there is a modest improvement in the good-fit criterion, the second time component is shorter than the IRF FWHM, which I call a sub-IRF component. In this case, I can tell that increasing the number of fitting parameters is physically meaningless for the fluorescence decay. Instead, this decay is better described by a single-exponential function, even though the good-fit criteria are not as perfect as I would like. The only situation where I would keep a fit that has a sub-IRF component is if increasing the number of fitting parameters leads to a drastic improvement in the good-fit criteria (e.g., the χ^2 changes from 500 to 1.5). Ultimately, determining the appropriate fit is very tricky

and requires a practiced and cautious eye. Once you finish this section, I provided a more rigorous exercise in the standard operating procedures in order to illustrate points discussed here. It would be in your best interest to carry out the exercise before fitting experimental data.

Aggregate Thin-Film Sample Explanation

I will briefly discuss some of the data obtained from thin-film samples to present fitting analysis in a physical context. The notable property about thin-film samples is that they were fitted by bi-exponential or multi-exponential functions.²⁴ That means there are multiple time components that are associated with a physical characteristic of the system and may allude to the heterogeneity of the sample. However, we need to characterize the overall decay by calculating the time-averaged lifetime according to: $\langle \tau \rangle = \frac{\sum \alpha_i \tau_i^2}{\sum \alpha_i \tau_i}$.¹⁵ Since I collected multiple decays for each dye-loading concentration, I took the average of all the $\langle \tau \rangle$ associated with a dye-loading concentration to state the overall $\langle \tau \rangle$.

The lifetimes of R560 in solution and adsorbed on a TiO₂ and ZrO₂ substrate were measured as a function of dye-loading concentration. Figure 1 presents the normalized emission decays of the different samples with the instrument response function (IRF, black, FWHM ~130 ps). R560 in acetonitrile serves as a standard for which there are available literature comparisons and has a $\langle \tau \rangle = 3.36 \pm 0.04$ ns, which is consistent with previous studies.²⁵ When we compare the $\langle \tau \rangle$ in solution to a thin film sample, we observe a decrease in

fluorescent lifetime and quenched fluorescence dynamics. In particular, there is a dye-loading concentration dependence of R560 and the lifetime, where 10^{-5} M is more quenched than 10^{-7} M, which indicates that aggregation at the higher dye-loading concentration may affect the lifetime and dynamics. Furthermore, we observe the effects of substrate, where TiO_2 fluorescence dynamics are quenched relative to ZrO_2 . This confirms that injection is occurring on the TiO_2 substrate, whereas ZrO_2 is known to inhibit injection. These overall lifetime decays provide a time-resolved window into the excited-state dynamics of R560, which will help improve our understanding of the competing ET kinetics.

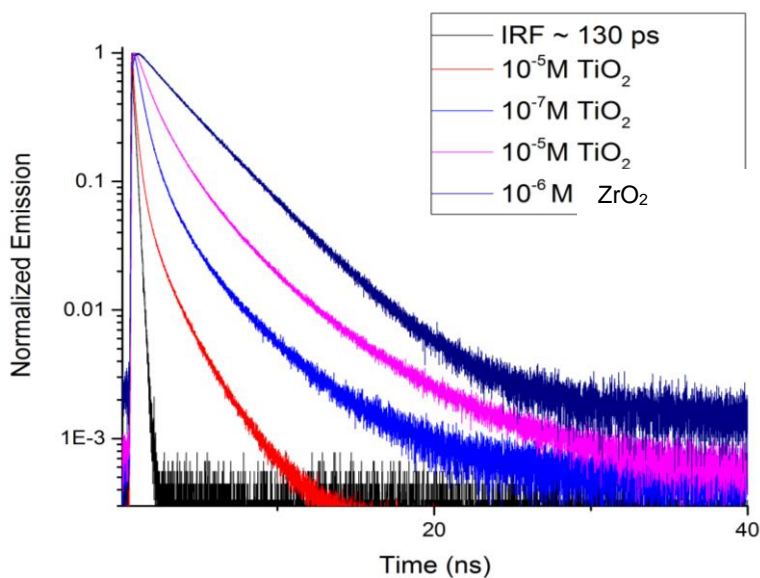


Figure 1. Normalized emission decay of R560 in solution and adsorbed onto TiO_2 and ZrO_2 substrates. IRF FWHM ~ 130 ps.

Future Work and Last Notes

TCSPC provides an abundance of information on the excited state, and we can couple it with SMS to improve our interpretation of excited-state dynamics and fluorescence. With the change point detection algorithm, single

molecules (SMs) are shown to have multiple emissive intensities.^{26,27} However, the origin of multiple emissive intensities is not well understood.^{26,27} Previous studies have shown that multiple emissive intensities from single molecules may be attributed to spectral diffusion or environmental fluctuations.²⁶ Yet, it is hypothesized that the multiple emissive intensities may be attributed to an evolution in the radiative and nonradiative decay constants of the excited state.²⁶ Future work will focus on combining SMS and TCSPC by simultaneously measuring blinking dynamics and collecting fluorescence lifetime decays.²⁸ This combined approach will enhance our ability to understand ET dynamics at the nanoscale level.

As mentioned in the introduction, this appendix should be accompanied by the TCSPC standard operating procedures. The set of standard operating procedures is essentially an instruction manual on setting up the microscope for TCSPC studies, taking measurements, using the Fluofit program, and working up figures along with various exercises. The appendix should provide rationales behind instructions taken to conduct TCSPC studies. Major references that lab researchers should refer to for greater TCSPC understanding should start with the tech manuals for the laser and TCSPC module,¹⁹⁻²¹ textbooks,^{15,16} fitting software manual,²² and the large lifetime study.²³ Understanding the combined SMS-TCSPC approach should begin with the textbooks,^{15,16} technical note,²⁸ and single-molecule study.²⁶

Acknowledgements

I would like to acknowledge the NASA Virginia Space Grant Consortium for their support through a Graduate Fellowship. I also thank Simran Rohatgi and James Cassidy for their help with control studies and samples to implement TCSPC and interpreting data.

References

1. Won Y.R.; Hojin J.; Ho-Sub K.; Woo-Jae C.; Jung S.S.; Bong-Hyun J. Recent Progress in Dye-Sensitized Solar Cells for Improving Efficiency: TiO₂ Nanotube Arrays in Active Layer. *Journal of Nanomaterials*. **2015**, 16, 1-17.
2. Listorti, A.; O'Regan, B.; Durrant, J. Electron Transfer Dynamics in Dye-Sensitized Solar Cells. *Chem. Mater.* **2011**, 23, 3381-3399.
3. Rao, G.V.; Dhital, B.; He, Y.; Lu, H.P. Single-Molecule Interfacial Electron Transfer Dynamics of Porphyrin on TiO₂ Nanoparticles: Dissecting the Complex Electronic Coupling Dependent Dynamics. *J. Phys. Chem. C*. **2014**, 118(35), 20209-20221
4. Asbury, J. B.; Ellingson, R. J.; Ghosh, H. N.; Ferrere, S.; Nozik, A. J.; Lian, T. Q. J. Femtosecond IR study of excited-state relaxation and electron-injection dynamics of Ru (dcbpy) 2 (NCS) 2 in solution and on nanocrystalline TiO₂ and Al₂O₃ thin films. *J. Phys. Chem. B*, **1999**, 103, 3110–3119.
5. Ramakrishna, G.; Jose, D. A.; Kumar, D. K.; Das, A.; Palit, D. K.; Ghosh, H. N. J. Strongly coupled ruthenium-polypyridyl complexes for efficient electron injection in dye-sensitized semiconductor nanoparticles. *J. Phys. Chem. B* **2005**, 109, 15445–15453.
6. Koops, S.E.; O'Regan, B.C.; Barnes, P.R.F.; Durrant, J.R. Parameters Influencing the Efficiency of Electron Injection in Dye-Sensitized Solar Cells. *JACS*, **2009**, 131 (13), 4808-4818.
7. Koops, S.E.; Barnes, P.R.F.; O'Regan, B.C.; Durrant, J.R. Kinetic Competition in a Coumarin Dye-Sensitized Solar Cell: Injection and Recombination Limitations upon Device Performance. *J. Phys. Chem. C.*, **2010**, 114(17), 8054-8061.
8. Santos, D.T.; Morandeira, A.; Koops, S.; Mozer, A.J.; Tskeouras, G.; Dong, Y.; Wagner, P. Wallace, G.; Earles, J.C.; Gordon, K.C.; Officer, D.; Durrant, J.R. Injection Limitations in a Series of Porphyrin Dye-Sensitized Solar Cells. *J. Phys. Chem. C.*, **2010**, 114(7), 3276-3279.
9. Sanchez-Diaz, A.; Martinez-Ferrero, E.; Palomares, E. Charge recombination studies in conformally coated trifluoroacetate/TiO₂ modified dye sensitized solar cells (DSSC). *J. Mater. Chem.* **2009**, 19, 5831-5387.
10. Roiait, V.; Colella, S.; Lerario, G.; De Marco, L.; Rizzo, A.; Listorti, A.; Gigli, G. Investigating charge dynamics in halide perovskite-sensitized mesostructured solar cells. *Energy Environ. Sci.* **2014**, 7, 1889-1894.
11. Wong, N.Z.; Ogata, A.F.; Wustholz, K.L. Dispersive Electron-Transfer Kinetics from Single Molecules on TiO₂ Nanoparticle Films. *J. Phys. Chem. C*. **2013**, 117(41), 21075-21085.
12. Ramakrishna, G.; Ghosh, H. N. Emission from the charge transfer state of xanthene dye-sensitized TiO₂ nanoparticles: A new approach to determining back electron transfer rate and verifying the Marcus inverted regime. *J. Phys. Chem. B* **2001**, 105, 7000–7008.
13. Benda, A.; Hof, M.; Wahl, M.; Patting, M.; Erdmann, R.; Kapusta, P. TCSPC upgrade of a confocal FCS microscope. *Rev. Sci. Instrum.* **2005**, 76, 033106.
14. Spinelli, A.; Ghioni, M.A.; Cova, S.D.; Davis, L.M. Avalanche Detector with Ultraclean Response for Time-Resolved Photon Counting. *IEEE Journal of Quantum Electronics*. **1998**, 34(5), 817-821.
15. Lakowicz, J.R. *Principles of Fluorescence Spectroscopy*; 3 ed.; Springer, **2006**.
16. O' Connor, D.V. and Phillips, D. *Time-Correlated Single Photon Counting*. Academic Press, London, **1984**.
17. Becker, W.; Berghmann, A. Timing Stability of TCSPC Experiments. *SPIE*. **2006**, 6372, 637209.
18. Kuhnemuth, R.; Seidel, C.A.M. *Principles of Single-Molecule Multiparameter Fluorescence Spectroscopy*. *Single Mol.* **2001**, 4, 251-254.
19. PicoQuant Tech Manual for the PDL 800-D LDH laser head and driver.
20. PicoQuant Tech Manual for the PicoHarp 300 module.
21. Wahl, M. Time-Correlated Single Photon Counting. PicoQuant Technical Note, **2014**, 1-14.

22. PicoQuant Tech Manual for Fluofit v. 4.6
23. Boens, N., Qin, W., Basarić, N., Hofkens, J., Ameloot, M., Pouget, J., Lefèvre, J.P., Valeur, B., Gratton, E., VandeVen, M., Silva, N.D. Fluorescence lifetime standards for time and frequency domain fluorescence spectroscopy. *Analytical chemistry*, **2007**, 79(5), 2137-2149.
24. Cassidy, J.P.; Tan, J.A.; Wustholz, K.L. Probing the Aggregation and Photodegradation of Rhodamine Dyes on TiO₂. *JPCC*, **2017**, Just Accepted.
25. Nagy, A.M., Talbot, F.O., Czar, M.F. and Jockusch, R.A. Fluorescence lifetimes of rhodamine dyes in vacuo. *Journal of Photochemistry and Photobiology A: Chemistry*, **2012**, 244, pp.47-53.
26. Bott, E.D., Riley, E.A., Kahr, B. and Reid, P.J. Unraveling the dispersed kinetics of dichlorofluorescein in potassium hydrogen phthalate crystals. *JPCA*, **2010**, 114(27), 7331-7337.
27. Tan, J.A., Rose, J.T., Cassidy, J.P., Rohatgi, S.K. and Wustholz, K.L. Dispersive Electron-Transfer Kinetics of Rhodamines on TiO₂: Impact of Structure and Driving Force on Single-Molecule Photophysics. *JPCC*, **2016**, 120(37), 20710-20720.
28. Wahl, M. Time Tagged Time-Resolved Fluorescence Data Collection in Life Sciences. PicoQuant Technical Note, **2014**, 1-10.